

Nuclear de-excitations in low-energy charged-current ν_e scattering on ^{40}Ar

Steven Gardiner^{1,2,*}

¹*Fermi National Accelerator Laboratory, Batavia, Illinois 60510 USA*

²*Department of Physics, University of California, Davis, California 95616 USA*

(Dated: January 16, 2022)

Background: Large argon-based neutrino detectors, such as those planned for the Deep Underground Neutrino Experiment, have the potential to provide unique sensitivity to low-energy (few to tens of MeV) electron neutrinos produced by core-collapse supernovae. Despite their importance for neutrino energy reconstruction, nuclear de-excitations following charged-current ν_e absorption on ^{40}Ar have never been studied in detail at supernova energies.

Purpose: I develop a model of nuclear de-excitations that occur following the $^{40}\text{Ar}(\nu_e, e^-)^{40}\text{K}^*$ reaction. This model is applied to the calculation of exclusive cross sections.

Methods: A simple expression for the inclusive differential cross section is derived under the allowed approximation. Nuclear de-excitations are described using a combination of measured γ -ray decay schemes and the Hauser-Feshbach statistical model. All calculations are carried out using a novel Monte Carlo event generator called MARLEY (Model of Argon Reaction Low Energy Yields).

Results: Various total and differential cross sections are presented. Two de-excitation modes, one involving only γ -rays and the other including single neutron emission, are found to be dominant at few tens-of-MeV energies.

Conclusions: Nuclear de-excitations have a strong impact on the achievable energy resolution for supernova ν_e detection in liquid argon. Tagging events involving neutron emission, though difficult, could substantially improve energy reconstruction. Given a suitable calculation of the inclusive cross section, the MARLEY nuclear de-excitation model may readily be applied to other scattering processes.

I. INTRODUCTION

Core-collapse supernovae are exceptionally intense sources of tens-of-MeV neutrinos and antineutrinos of all flavors. In a typical supernova, about 10^{58} neutrinos are released in a burst lasting tens of seconds. Although the first observation of supernova neutrinos by the Kamiokande-II [1], Baksan [2], and Irvine-Michigan-Brookhaven [3] detectors in 1987 yielded a total of only two dozen events, the scientific impact of this dataset has been tremendous, leading to numerous publications on a wide variety of subjects [4–9]. In the years since first detection, a worldwide network of large neutrino experiments, most built primarily for other applications, stands ready to perform a second, high-statistics measurement if a core-collapse supernova should occur within the galaxy [10]. Due to the slow rate of galactic core-collapse supernovae (estimated to be about 1.6 per century [11]), the prospect of such a measurement represents a rare but valuable opportunity to shed light on the details of core-collapse and nucleosynthesis, study neutrinos under extreme conditions, search for evidence of physics beyond the Standard Model, and explore many other topics [12–14].

A full realization of the physics potential of the next galactic core-collapse supernova will require a simultaneous measurement of neutrinos of all flavors. While detectors based on water and hydrocarbon scintillator will primarily detect $\bar{\nu}_e$ via inverse beta decay (IBD)

$$\bar{\nu}_e + p \rightarrow e^+ + n, \quad (1)$$

liquid-argon-based detectors are anticipated to provide unique sensitivity [15, 16] to ν_e via the charged-current (CC) reaction

$$\nu_e + ^{40}\text{Ar} \rightarrow e^- + ^{40}\text{K}^* \quad (2)$$

which dominates the expected signal at supernova energies.

Within the decade, the Deep Underground Neutrino Experiment (DUNE) will begin operating four ten-kiloton liquid argon time projection chambers (LArTPCs) with the primary goals of studying long-baseline oscillations of accelerator neutrinos, searching for proton decay, and measuring the ν_e flux from a galactic core-collapse supernova if one should occur during the lifetime of the experiment [17]. Initial studies of the sensitivity of DUNE to supernova neutrinos, performed by the collaboration itself [15] and by smaller groups (e.g., ref. [18]) show promise, and the potential exists for measurements by DUNE of other low-energy neutrinos, notably those produced by the Sun [19].

In addition to DUNE, three sub-kiloton LArTPCs, SBND [20, 21], MicroBooNE [22], and ICARUS [23], are currently operating or being installed in the Booster Neutrino Beam at Fermilab. A joint effort between the three experimental collaborations, known as the Short Baseline Neutrino (SBN) program [24, 25], will perform precision measurements of neutrino oscillations. In addition to this primary mission, the SBN detectors will pursue a variety of other physics measurements and are expected to be sensitive to supernova neutrinos. To ensure that data from a core-collapse supernova would be fully recorded over the ten-second burst, the MicroBooNE collaboration operates a first-of-its-kind continuous readout stream and

* gardiner@fnal.gov

has demonstrated its capabilities via reconstruction of Michel electrons produced by decays of cosmic muons [26].

While much remains to be done to fully exploit the low-energy capabilities of LArTPCs, a first demonstration by the ArgoNeuT [27] experiment of reconstruction of MeV-scale activity due to accelerator-neutrino-induced neutrons and de-excitation γ -rays achieved a detection threshold of around 200–300 keV [28]. These encouraging initial results have prompted further experimental work by MicroBooNE [29] and multiple simulation-based studies considering the implications for reconstruction of both high- and low-energy physics events [30, 31].

In future analyses of supernova neutrino data, the event-by-event reconstructed neutrino energy obtained by each detector will be of primary interest. For IBD events in water or scintillator, because only a single hadronic final state (a free neutron) is accessible at tens-of-MeV energies, a measurement of the outgoing positron energy is sufficient to reconstruct the antineutrino energy with high accuracy. Due to the use of a complex nuclear target (argon) in LArTPCs, however, various nuclear transitions may occur in response to CC ν_e absorption, and thus a one-to-one mapping (up to nuclear recoil) between the neutrino and electron energies no longer exists.

To fully reconstruct the neutrino energy in the argon case, the reaction Q-value, i.e., the energy imparted to the nuclear transition, must be inferred by detecting the nuclear de-excitation products. For transitions to bound nuclear energy levels, the neutrino energy is in principle fully recoverable by measuring the energies of all de-excitation γ -rays in addition to the primary electron. For transitions to unbound nuclear states, a model is needed to correct for missing energy associated with undetected nuclear fragments. In practice, an experimental analysis that attempts to isolate the simpler bound transitions will also need a detailed de-excitation model in order to estimate the purity of the event selection.

With the exception of a recent first measurement [32] of coherent elastic neutrino-nucleus scattering, experimental data have not yet been obtained for neutrino-argon cross sections in the supernova energy regime. Furthermore, only a few measurements with limited precision are available for low-energy inelastic neutrino scattering on any nuclear target [33, table 3]. Despite this, a substantial literature exists for theoretical calculations of the $^{40}\text{Ar}(\nu_e, e^-)^{40}\text{K}^*$ process. A review through 2018 is provided in ref. [34, sec. 7.1], with a notable recent addition being two publications [35, 36] which employ a Continuum Random Phase Approximation (CRPA) model to study this cross section above the nucleon emission threshold.

While highly useful for providing competing estimates of event rates in DUNE and other argon-based detectors, all published calculations for this cross section to date share the limitation of being fully inclusive, i.e., predictions are made that consider only the kinematics

of the outgoing electron. At very low neutrino energies, where only transitions to bound nuclear states are possible, this is not problematic: measured de-excitation γ -ray branching ratios exist for many levels of the daughter ^{40}K nucleus, and missing data may be addressed using straightforward theoretical estimates. However, above about 15–20 MeV, kinematic access to unbound nuclear states becomes appreciable, and a detailed treatment of the competition between various de-excitation channels (including emission of both γ -rays and nuclear fragments) is needed.

Although such a treatment has not previously been provided for ^{40}Ar , detailed modeling of nuclear de-excitations induced by low-energy neutrino interactions has been pursued for a number of other nuclei [37–42]. A universal assumption made by all of these calculations (as well as the present work) is that of *compound nucleus* formation: following the primary interaction, the nucleus is left in a thermally-equilibrated excited state that decays independently of the details of its formation process. While further work is needed to fully investigate the adequacy of this assumption for low-energy neutrino-nucleus reactions, both theoretical calculations [43, 44] and electron scattering data [45] suggest that compound processes dominate over the direct nucleon knock-out important at higher energies.

In this paper, I present the first calculations at tens-of-MeV energies for cross sections for exclusive final states of the reaction $^{40}\text{Ar}(\nu_e, e^-)^{40}\text{K}^*$, emphasizing the role of nuclear de-excitation processes. In section II, I develop a simple model for the inclusive differential cross section, relying on approximations that work best at low momentum transfers. The derivation in section II fully determines the cross section up to the values of two (Fermi and Gamow-Teller) nuclear matrix elements, $B(F)$ and $B(GT)$, which are considered in section III. While relevant neutrino scattering data are currently unavailable, the needed values of these matrix elements at low excitation energies may be extracted from measurements of related processes. I supplement these measurements with the results of a theoretical calculation at high excitation energies to obtain a full treatment of the inclusive cross section. In section IV, I describe a detailed model of nuclear de-excitations that can be used together with the inclusive cross section to obtain predictions for exclusive final states. In section V, I present example results calculated using the models developed in the previous sections.

To enable practical calculations that have already helped to inform studies of DUNE’s sensitivity to supernova neutrinos [15], all of the physics models described herein have been implemented in a new Monte Carlo event generator called **MARLEY** (Model of Argon Reaction Low Energy Yields). All results shown in this work may be reproduced using version 1.2.0 of **MARLEY** [46], which is publicly available as an open-source software project [47]. Documentation of the technical details of **MARLEY** and usage instructions are available in ref. [48].

Due to the compound nucleus assumption, the MARLEY de-excitation model may easily be used in the future to provide exclusive predictions for a more refined calculation of the inclusive CC ν_e absorption cross section for ^{40}Ar . A similar approach to modeling de-excitations for other reaction modes and target nuclei is likewise possible, and I welcome potential collaboration on this topic. Prospects for improving MARLEY predictions beyond the proof-of-concept reported here are briefly considered in section VI.

II. INCLUSIVE CROSS SECTION MODEL

For momentum transfers that are small compared to the W boson mass, the tree-level amplitude \mathcal{M} for inclusive charged-current neutrino-nucleus scattering may be represented diagrammatically as

$$i\mathcal{M} = \quad (3)$$

The corresponding differential cross section may be written in the form

$$\frac{d\sigma}{dQ^2} = \frac{G_F^2 |V_{ud}|^2}{32\pi (s - m_i^2)^2} F_C L_{\mu\nu} W^{\mu\nu}, \quad (4)$$

where $q = k - k' = p' - p$ is the four-momentum transfer, $Q^2 \equiv -q^2$, G_F is the Fermi constant, V_{ud} is the Cabibbo–Kobayashi–Maskawa matrix element connecting the up and down quarks, Mandelstam s is the square of the total energy in the center-of-momentum (CM) frame, and m_i is the mass of the initial-state nucleus. Discussion of the Coulomb correction factor F_C is deferred to section II B.

The leptonic ($L_{\mu\nu}$) and hadronic ($W^{\mu\nu}$) tensors are defined by

$$L_{\mu\nu} \equiv \text{Tr}[\gamma_\mu (1 - \gamma_5) \not{k}' \gamma_\nu (1 - \gamma_5) (\not{k} + m_\ell)] \quad (5)$$

$$= 8 [k_\mu k'_\nu + k_\nu k'_\mu - g_{\mu\nu} (k \cdot k') - i\epsilon_{\mu\nu\rho\sigma} k^\rho k'^\sigma] \quad (6)$$

and

$$W^{\mu\nu} \equiv \frac{1}{2J_i + 1} \sum_{M_i} \sum_{M_f} \mathcal{N}^\mu \mathcal{N}^{\nu*}. \quad (7)$$

Here m_ℓ is the mass of the final-state lepton, J_i (J_f) is the initial (final) nuclear spin, and M_i (M_f) is the third

component of the nuclear spin in the initial (final) state.

Under the impulse approximation, the nuclear matrix element may be written in coordinate space as

$$\mathcal{N}^\mu = \langle f | \sum_{n=1}^A e^{i\mathbf{q} \cdot \mathbf{x}(n)} j^\mu(n) | i \rangle \quad (8)$$

where \mathbf{q} is the three-momentum transfer and the sum runs over all A nucleons. The weak current operator $j^\mu(n)$ is understood to act only on the n th nucleon, as is the position operator $\mathbf{x}(n)$. The state vectors in eq. (8) are normalized relativistically, i.e.,

$$\langle i | i \rangle = 2E_i \quad \langle f | f \rangle = 2E_f \quad (9)$$

where E_i (E_f) is the total energy of the nucleus in the initial (final) state. Equation (4) contains an implied sum over the accessible final nuclear states.

A. Allowed approximation

The full expression for the single-nucleon weak current operator j^μ is well-known and is given in ref. [34] among other places. For this study, however, I evaluate the current operator in the *allowed approximation*, which combines the long-wavelength ($q \rightarrow 0$) limit and the slow-nucleon limit (in which the momentum of the initial struck nucleon is neglected compared to its mass).

Under this approximation, the weak current operator reduces to the simple form

$$j^0 = g_V t_- \quad j^a = -\sigma^a g_A t_- \quad (10)$$

where j^0 is the time component and the three Cartesian spatial components are labeled with $a \in \{1, 2, 3\}$. The time component of the nuclear matrix element \mathcal{N}^μ is given by

$$\mathcal{N}^0 = \frac{g_V}{\sqrt{2J_i + 1}} \delta_{J_i J_f} \delta_{M_i M_f} \langle f | \mathcal{O}_F | i \rangle \quad (11)$$

while the spatial components may be written in spherical coordinates as

$$\mathcal{N}^w = \frac{-g_A (-1)^{J_i - M_i}}{\sqrt{3}} (J_f M_f J_i - M_i | 1 w) \langle f | \mathcal{O}_{GT} | i \rangle \quad (12)$$

where $w \in \{-1, 0, 1\}$ and g_V (g_A) is the vector (axial-vector) weak coupling constant of the nucleon. The Fermi (F) and Gamow-Teller (GT) operators are defined by

$$\mathcal{O}_F \equiv \sum_{n=1}^A t_-(n) \quad (13)$$

$$\mathcal{O}_{GT} \equiv \sum_{n=1}^A \boldsymbol{\sigma}(n) t_-(n) \quad (14)$$

where $\boldsymbol{\sigma}$ is the Pauli vector, and t_- , the isospin-lowering

operator, converts a neutron into a proton. Double bars ($\|\|$) denote matrix elements which have been reduced via the Wigner-Eckhart theorem.

Equations (11) and (12) may be used to evaluate the elements of the hadronic tensor $W^{\mu\nu}$. Under the allowed approximation, these become

$$W^{00} = 4 E_i E_f B(F) \quad (15)$$

$$W^{ab} = \frac{4}{3} \delta_{ab} E_i E_f B(GT) \quad (16)$$

$$W^{0a} = W^{a0} = 0 \quad (17)$$

where the reduced Fermi and Gamow-Teller matrix ele-

ments are given by

$$B(F) \equiv \frac{g_V^2}{2J_i + 1} \left| \langle J_f \| \mathcal{O}_F \| J_i \rangle \right|^2 \quad (18)$$

$$B(GT) \equiv \frac{g_A^2}{2J_i + 1} \left| \langle J_f \| \mathcal{O}_{GT} \| J_i \rangle \right|^2. \quad (19)$$

The state vectors labeled using the nuclear spin (J_i or J_f) are normalized to unity:

$$\langle J_i | J_i \rangle = \langle J_f | J_f \rangle = 1. \quad (20)$$

The reduced matrix elements satisfy the spin-parity selection rules

$$B(F) = 0 \text{ unless } J_f = J_i \text{ and } \Pi_f = \Pi_i \quad (21)$$

and

$$B(GT) = 0 \text{ unless } |J_i - 1| \leq J_f \leq J_i + 1 \text{ and } \Pi_f = \Pi_i. \quad (22)$$

where Π_i (Π_f) is the initial (final) nuclear parity.

Combining the results above leads to the following expression for the allowed approximation differential cross section in the CM frame:

$$\frac{d\sigma}{d\cos\theta_\ell} = \frac{G_F^2 |V_{ud}|^2}{2\pi} F_C \left[\frac{E_i E_f}{s} \right] E_\ell |\mathbf{p}_\ell| \left[\left(1 + \beta_\ell \cos\theta_\ell \right) B(F) + \left(1 - \frac{1}{3} \beta_\ell \cos\theta_\ell \right) B(GT) \right]. \quad (23)$$

Here E_ℓ , \mathbf{p}_ℓ , θ_ℓ , and $\beta_\ell = E_\ell/|\mathbf{p}_\ell|$ are, respectively, the total energy, three-momentum, scattering angle, and speed of the final-state lepton. The factor $E_i E_f/s$ accounts for nuclear recoil and is commonly neglected.

In the CM frame, the particle energies are independent of the scattering angle θ_ℓ . As a result, integration of the total cross section is trivial and leads to the expression

$$\sigma = \frac{G_F^2 |V_{ud}|^2}{\pi} F_C \left[\frac{E_i E_f}{s} \right] E_\ell |\mathbf{p}_\ell| \left[B(F) + B(GT) \right]. \quad (24)$$

As was the case for eq. (4), the cross-section formulas in eqs. (23) and (24) contain an implicit sum over nuclear final states.

B. Coulomb corrections

Final-state interactions (FSIs) of the outgoing charged lepton with the Coulomb field of the nucleus have a significant effect on the cross section at low energies. While a detailed treatment of Coulomb FSIs is achievable via the distorted-wave Born approximation, a much more convenient approximation scheme based on the work of Engel

[49] is typically used, e.g., in refs. [35, 50, 51].

Under this approach, the Coulomb correction factor F_C that appears in eqs. (4), (23) and (24) is calculated using either the Fermi function [52, 53] or the modified effective momentum approximation (MEMA) [49]. Since the former is known to overestimate Coulomb corrections at high lepton energies while the latter does the same at low energies, the smaller of the two alternatives is always chosen. This amounts to defining the Coulomb correction factor as

$$F_C \equiv \begin{cases} F_{\text{Fermi}} & |F_{\text{Fermi}} - 1| < |F_{\text{MEMA}} - 1| \\ F_{\text{MEMA}} & \text{otherwise} \end{cases} \quad (25)$$

where the Fermi function is given by

$$F_{\text{Fermi}} = \frac{2(1+S)}{[\Gamma(1+2S)]^2} (2\gamma_{\text{rel}} \beta_{\text{rel}} m_\ell R)^{2S-2} e^{-\pi\eta} |\Gamma(S - i\eta)|^2 \quad (26)$$

and

$$F_{\text{MEMA}} \equiv \frac{\mathcal{K}_{\text{eff}} \mathcal{E}_{\text{eff}}}{\mathcal{K} \mathcal{E}}. \quad (27)$$

In eq. (26) the quantity S is defined in terms of the fine structure constant α by

$$S \equiv \sqrt{1 - \alpha^2 Z_f^2} \quad (28)$$

where Z_f is the proton number of the final nucleus. The nuclear radius (in natural units) may be estimated as

$$R \approx \frac{1.2 A^{1/3} \text{ fm}}{\hbar c}, \quad (29)$$

and the Sommerfeld parameter η is given by

$$\eta = \frac{\alpha Z_f z_\ell}{\beta_{\text{rel}}}. \quad (30)$$

where z_ℓ is the electric charge (in units of the elementary charge) of the final-state lepton.

Typical presentations of the correction factors defined in eqs. (26) and (27) neglect the small recoil kinetic energy of the final nucleus in the laboratory frame. This allows the use of expressions for F_{Fermi} and F_{MEMA} which are derived in the rest frame of the final nucleus. I opt instead for Lorentz-invariant forms of the correction factors written in terms of the relative speed β_{rel} of the two final-state particles: [54]

$$\beta_{\text{rel}} = \frac{\sqrt{(k' \cdot p')^2 - m_\ell^2 m_f^2}}{k' \cdot p'} \quad \gamma_{\text{rel}} \equiv (1 - \beta_{\text{rel}}^2)^{-1/2}. \quad (31)$$

The symbols \mathcal{E} and \mathcal{K} from eq. (27) denote, respectively, the total energy and momentum of the outgoing lepton in the rest frame of recoiling nucleus:

$$\mathcal{E} \equiv \gamma_{\text{rel}} m_\ell \quad \mathcal{K} \equiv \beta_{\text{rel}} \mathcal{E}. \quad (32)$$

The *effective* values of these variables are those that exist in the presence of the nuclear Coulomb potential

$$\mathcal{K}_{\text{eff}} \equiv \sqrt{\mathcal{E}_{\text{eff}}^2 - m_\ell^2} \quad \mathcal{E}_{\text{eff}} \equiv \mathcal{E} - V_C(0), \quad (33)$$

which is approximated by that at the center of a uniformly-charged sphere:

$$V_C(0) \approx \frac{3 Z_f z_\ell \alpha}{2 R}. \quad (34)$$

It should be noted that, as originally presented [49], the MEMA also involves modifying the value of the momentum transfer used to evaluate the amplitude \mathcal{M} . Since the cross section treatment presented here involves use of the long-wavelength limit $q \rightarrow 0$, however, I neglect this additional correction.

III. ALLOWED NUCLEAR MATRIX ELEMENTS

Despite sustained community interest and a concrete proposal by the CAPTAIN experiment [55] to perform direct measurements, no experimental data for tens-of-MeV charged-current ν_e scattering on argon are currently available. However, in recent decades, three separate experiments have obtained values of the allowed matrix elements $B(F)$ and $B(GT)$ by considering related physics processes.

The first two experiments were performed in the late 1990s by separate teams working at the Gesellschaft für Schwerionenforschung (Society for Heavy Ion Research) in Darmstadt, Germany [56] and the Grand Accélérateur National d'Ions Lourds (Large Heavy Ion National Accelerator) in Caen, France [57]. Both sought to study CC ν_e absorption on ^{40}Ar by measuring beta decays of its mirror nucleus ^{40}Ti :

$$^{40}\text{Ti} \rightarrow ^{40}\text{Sc}^* + e^+ + \nu_e. \quad (35)$$

In the limit of perfect isospin symmetry, the matrix element describing a ^{40}Ti beta decay transition to a specific ^{40}Sc level is equal to the matrix element accessing the level's isobaric analog in ^{40}K via CC ν_e scattering on ^{40}Ar . The main difficulties in applying this technique to neutrino cross sections are (1) the beta decay Q-value limits the maximum excitation energy that may be studied, and (2) energy levels in the beta decay daughter nucleus (^{40}Sc) must be matched to their analogs in the final-state nucleus for neutrino scattering (^{40}K).

The third experiment [58], performed about a decade later at the Indiana University Cyclotron Facility, extracted $B(GT)$ values from measurements of (p,n) scattering on ^{40}Ar . The extraction technique relied on the observation, first put forward in 1980 [59] and subsequently refined [60–62], that the (p,n) cross section at very forward angles ($\theta \approx 0^\circ$) for proton energies around 100 MeV is approximately proportional to the allowed matrix elements $B(F)$ and $B(GT)$. While subject to some unique difficulties of its own (see, e.g., ref. [63, sec. 4.2]), this approach overcomes key limitations of ^{40}Ti beta decay: transitions to excited levels of ^{40}K may be studied directly at energies higher than the mirror beta decay Q-value.

A. Re-evaluation of existing measurements

Reasonable attempts were made in the original publications describing these measurements to assign the extracted matrix elements to known ^{40}K levels satisfying the spin-parity selection rules in eqs. (21)–(22). That is, the ^{40}K isobaric analog state accessed via a Fermi transition must have $J^\pi = 0^+$, while GT transitions may only populate levels with $J^\pi = 1^+$. However, in light of new ^{40}K level data that became available in 2017 [64], I re-

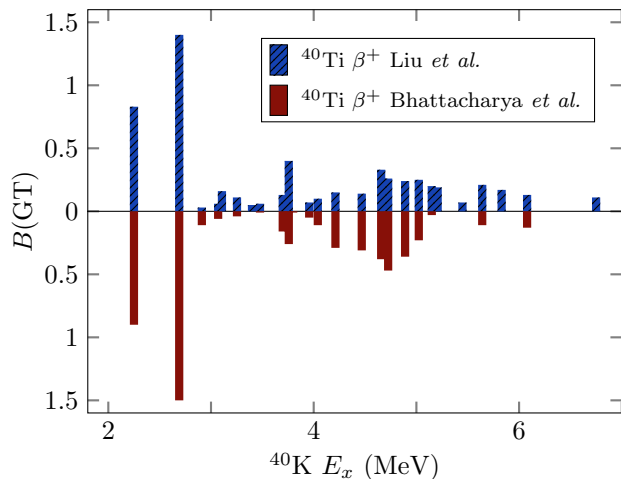


FIG. 1: Gamow-Teller strengths $B(\text{GT})$ from two independent measurements of $^{40}\text{Ti } \beta^+$ decay by Liu *et al.* [56] and Bhattacharya *et al.* [57].

visited the level assignments for all three measurements.

The results of this re-evaluation are shown in table I. Level energies (keV) and spin-parity assignments retrieved from the Evaluated Nuclear Structure Data File (ENSDF) database [65] are listed in the first and second columns, respectively. Excitation energies (for either ^{40}Sc or ^{40}K as appropriate) and matrix element values are listed in the following columns for each of the three experimental measurements. In the case of the (p,n) scattering data, the matrix element values provided in the original paper [58] have been scaled by a factor of $g_A^2 = 1.26^2$. This scaling was done because the definition of $B(\text{GT})$ used by the experiment does not include the axial-vector weak coupling constant g_A . The specific value $g_A = 1.26$ was chosen for consistency with the one assumed in the experimental analysis.

Figure 1 shows the Gamow-Teller strengths obtained by the two ^{40}Ti beta decay experiments mentioned previously. Excitation energies of analog states in ^{40}K , represented on the horizontal axis, are chosen to match the assignments made in table I. The vertical axis is inverted for the second dataset to facilitate comparisons. Rough consistency is seen between the two measurements, although the results reported by Liu *et al.* involve several more nuclear levels.

Figure 2 uses a similar format to individually compare each beta decay measurement to the GT strengths extracted from (p,n) scattering. Substantially more fragmentation of the strength is seen in the beta decay data, and there are areas of significant tension. For instance, the two experimental methods disagree on whether the GT strength to the ^{40}K level at 2.3 MeV is larger or smaller than the strength to the level at 2.7 MeV.

Differences between the beta decay and (p,n) data were examined in detail by Karakoç *et al.* in 2014 [67]. Based on a combination of theoretical calculations and a cur-

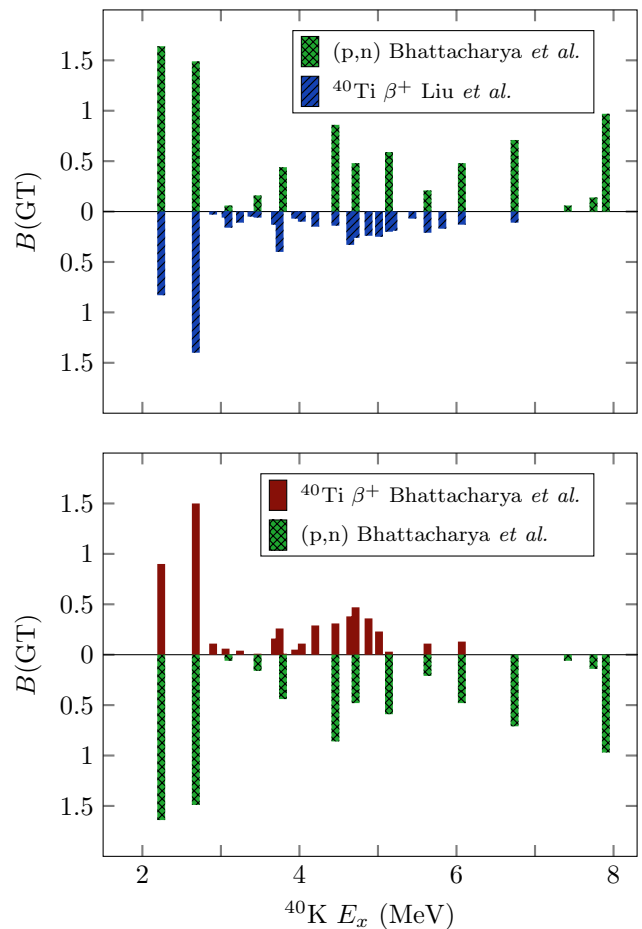


FIG. 2: Comparison of the Gamow-Teller strengths $B(\text{GT})$ measured using ^{40}Ti beta decay (see fig. 1) with those obtained using a measurement of 0° (p,n) scattering by Bhattacharya *et al.* [58].

rently unpublished $^{40}\text{Ar}(h, t)^{40}\text{K}$ measurement, the authors argued that the (p,n) data should be preferred over the ^{40}Ti beta decay data for calculations of CC ν_e absorption cross sections on argon. Rather than attempt to adjudicate between the conflicting datasets, I have opted to allow each of the three measurements to be used as a source of $B(\text{GT})$ values in MARLEY cross-section calculations.

B. Extension to higher excitation energies

Beyond the maximum excitation energy of about 8 MeV probed by the experiments mentioned in the previous section, the presence of additional Gamow-Teller strength is predicted by the model-independent Ikeda sum rule [68]. This rule states that the summed GT strength S_{GT}^- (S_{GT}^+) over all possible nuclear final states for CC ν_e ($\bar{\nu}_e$) absorption satisfies the relation

$$\Delta S_{\text{GT}} \equiv S_{\text{GT}}^- - S_{\text{GT}}^+ = 3g_A^2 (N_i - Z_i) \quad (36)$$

TABLE I: Level assignments and measured $B(F)$ and $B(GT)$ values for $^{40}\text{Ar}(\nu_e, e^-)^{40}\text{K}^*$

Assigned ^{40}K E_x (keV)	ENSDF [64] spin-parity assignment ^a	Liu <i>et al.</i> [56] ^{40}Ti β^+ decay		Bhattacharya <i>et al.</i> [57] ^{40}Ti β^+ decay		Bhattacharya <i>et al.</i> [58] $^{40}\text{Ar}(p, n)^{40}\text{K}$	
		^{40}Sc E_x (keV)	$B(F) +$ $B(GT)$	^{40}Sc E_x (keV)	$B(F) +$ $B(GT)$	^{40}K E_x (keV)	Weak ^b $B(GT)$
2289.868(11)	1^+	2287(10)	0.83(8)	2281(8)	0.90(4)	2333(30)	1.64(16)
2730.357(19)	1	2761(10)	1.40(10)	2752(8)	1.50(6)	2775(30)	1.49(14)
2950.9(6)		2966(40)	0.03(1)	2937(13)	0.11(2)		
3109.56(4)	$1^+, 2^+$	3121(46)	0.06(3)	3143(20)	0.06(1)		
3146.50(5)	$1^{(-)}$	3235(50)	0.16(4)			3204(32)	0.06(2)
3293(10)	unnatural ^c	3342(40)	0.11(8)	3334(19)	0.04(1)		
3439.18(3)	(2^+)	3418(60)	0.05(2)				
3517(15)		3521(40)	0.06(2)	3569(56)	0.01(1)	3503(30)	0.16(2)
3738.49(3) ^d	1^+	3662(40)	0.13(7)	3652(10)	0.16(2)		
3797.48(3)	1^+	3782(40)	0.40(16)	3786(10)	0.26(3)		
3840.27(3)	$(1, 2^+)$			3861(49)	0.01(1)	3870(30)	0.44(5)
3996(10)	unnatural ^c	4033(88)	0.07(4)	4067(24)	0.05(2)		
4080(5)		4194(60)	0.10(6)	4111(30)	0.11(3)		
4251.70(15)	$(1, 2^-)$	4264(46)	0.15(4)	4267(10)	0.29(3)		
4383.7(7) ^e	0^+	4365(10)	4.01(31)	4364(8)	3.84(17)		
4508(15)		4540(86)	0.14(5)	4522(16)	0.31(5)	4421(30)	0.86(14)
4697(10)	unnatural ^c	4628(40)	0.33(9)	4655(12)	0.38(6)		
4765(5)	$(1)^+$	4782(60)	0.26(11)	4825(21)	0.47(8)	4763(30)	0.48(5)
4930(10)	unnatural ^c	4997(72)	0.24(10)	5017(27)	0.36(9)		
5063.37(7)	$(2^-, 3^+)$	5051(40)	0.25(11)	5080(35)	0.23(7)		
5189.89(5)	(2^-)	5135(86)	0.20(6)	5223(32)	0.03(3)	5162(30)	0.59(6)
5247.1(6)		5362(60)	0.19(7)				
5488.65(17)	$(2^-, 3, 4^-)$	5574(40)	0.07(4)				
5681(32)		5777(60)	0.21(15)	5696(23)	0.11(4)	5681(32)	0.21(3)
5870(20)		5886(80)	0.17(7)				
6118(30)		6126(60)	0.13(7)	6006(21)	0.13(5)	6118(30)	0.48(5)
6790(30)		6426(60)	0.11(6)			6790(30)	0.71(8)
7468(37)						7468(37)	0.06(2)
7795(33)						7795(33)	0.14(2)
7952(32)						7952(32)	0.97(10)
Total ^f $B(GT)$			5.84(39)		5.52(20)		8.29(31)

^a Parenthesized values are based upon weak arguments [66].^b The data tabulated in ref. [58] were multiplied by $g_A^2 = 1.26^2$ to obtain the $B(GT)$ values shown here.^c A nuclear level with parity Π and spin J has *natural parity* if $\Pi = (-1)^J$. Otherwise it has *unnatural parity*.^d Another candidate ^{40}K level for this transition has $E_x = 3663.88$ keV and $J^\pi = (1^-, 2, 3, 4^+)$.^e This level is the isobaric analog of the ^{40}Ar ground state.^f Gamow-Teller transitions are assumed for all levels other than the isobaric analog state.

where $N_i = 22$ ($Z_i = 18$) is the neutron (proton) number of the initial ^{40}Ar nucleus. Equation (36) implies a minimum possible value of $S_{\text{GT}}^- = 12 g_A^2 \approx 19$ for the integrated GT strength associated with the reaction $^{40}\text{Ar}(\nu_e, e^-)^{40}\text{K}^*$. Comparing this value to the measured total GT strengths listed in the final row of table I reveals that the majority of the expected GT strength for CC ν_e absorption on ^{40}Ar is unmeasured and associated with transitions to high-lying, nucleon-unbound states of ^{40}K .

To supplement the experimental measurements with an estimate of the remainder of the GT strength, I rely on a Quasiparticle Random Phase Approximation (QRPA) calculation by Cheoun, Ha, and Kajino [69]. To avoid double-counting, theoretical GT matrix elements are included with the experimental ones only for excitation energies at which the integrated QRPA GT strength exceeds the experimental total.

C. Adopted matrix elements

Figure 3 presents three complete sets of allowed $^{40}\text{Ar}(\nu_e, e^-)^{40}\text{K}^*$ nuclear matrix elements prepared as input for MARLEY based on the measurements and QRPA prediction discussed above. The experimental $B(\text{GT})$ values are shown as green, red, or blue bars depending on the dataset. The theoretical QRPA $B(\text{GT})$ values are shown in violet.

In addition to extracting GT strengths, both beta decay experiments measured values of the Fermi matrix element $B(\text{F})$. Under the approximation that isospin is a good quantum number, this matrix element is expected to have the value

$$B(\text{F}) = g_V^2(N_i - Z_i) = 4 \quad (37)$$

and to connect the ground state of ^{40}Ar to a single 0^+ isobaric analog state in ^{40}K , which has been identified as the level with excitation energy $E_x = 4.3837$ MeV. Since the experimental data are fully consistent with these expectations, I adopt the value $B(\text{F}) = 4$ for this transition in all three sets of MARLEY matrix elements. The known Fermi transition is represented in each panel of Figure 3 by a white bar with horizontal hatch marks. Transitions to all other nuclear levels are assumed to proceed via the Gamow-Teller operator.

Although the differences become important at neutrino energies near threshold, the observables predicted in this paper are largely insensitive to the choice between the three sets of MARLEY matrix elements for the $^{40}\text{Ar}(\nu_e, e^-)^{40}\text{K}^*$ reaction. For definiteness, all MARLEY calculations shown in this work (see section V) are obtained using the `ve40ArCC.Bhattacharya1998.react` input file, which contains the matrix elements shown in the middle panel of fig. 3.

IV. NUCLEAR DE-EXCITATION MODEL

To model nuclear de-excitations following CC ν_e absorption on ^{40}Ar , I rely on the observation that, due to the selection rules in eqs. (21) and (22), each nuclear final state accessed by the neutrino interaction has a well-defined excitation energy, spin, and parity. Distinct treatments are used for bound and unbound nuclear states, with the latter being those for which the excitation energy exceeds the separation energy for at least one nuclear fragment with mass number $A \leq 4$. Separation energies are computed in MARLEY using atomic and particle mass data from refs. [70, 71]. Untabulated atomic masses are estimated using the liquid drop model of Myers and Swiatecki [72, 73]. The full de-excitation cascade is treated as a sequence of binary decays while neglecting the possibility of fission and emission of heavy nucleon clusters ($A \geq 5$).

A. Bound states: discrete level data

De-excitations of bound nuclear states are handled in MARLEY using a set of nuclear structure data files originally prepared for use with version 1.6 of the TALYS [74–76] nuclear reaction code.¹ These in turn are based on the level schemes included in version 3 of the Reference Input Parameter Library (RIPL-3) [78]. For a large number of nuclei, the files provide tables of discrete nuclear energy levels including their excitation energies, spin-parities, and de-excitation γ -ray branching ratios. Missing experimental measurements of these quantities are supplemented by theoretical estimates. Although internal conversion coefficients are provided in the TALYS data files, this process is neglected in MARLEY 1.2.0. In the unusual case where discrete level data are not available for a particular nuclide, γ -ray emission is simulated in the same manner as for unbound nuclear states.

The TALYS structure data files are used with minor reformatting for all nuclides except ^{40}K . To ensure consistency with the level assignments made in section III A, I prepared an original decay scheme for ^{40}K using the experimental data in ref. [64], the TALYS 1.6 structure file, and (where needed) estimated γ -ray branching ratios computed using the strength function defined in section IV B 3.

¹ The current release of TALYS is version 1.95. However, beginning with TALYS 1.8, some nuclear levels for nuclei with an odd mass number (e.g., ^{39}K) appear in the structure data files with an unphysical integer spin (as opposed to a half-integer spin). This bug, which remains unfixed [77], has prevented updates to the data files distributed with MARLEY.

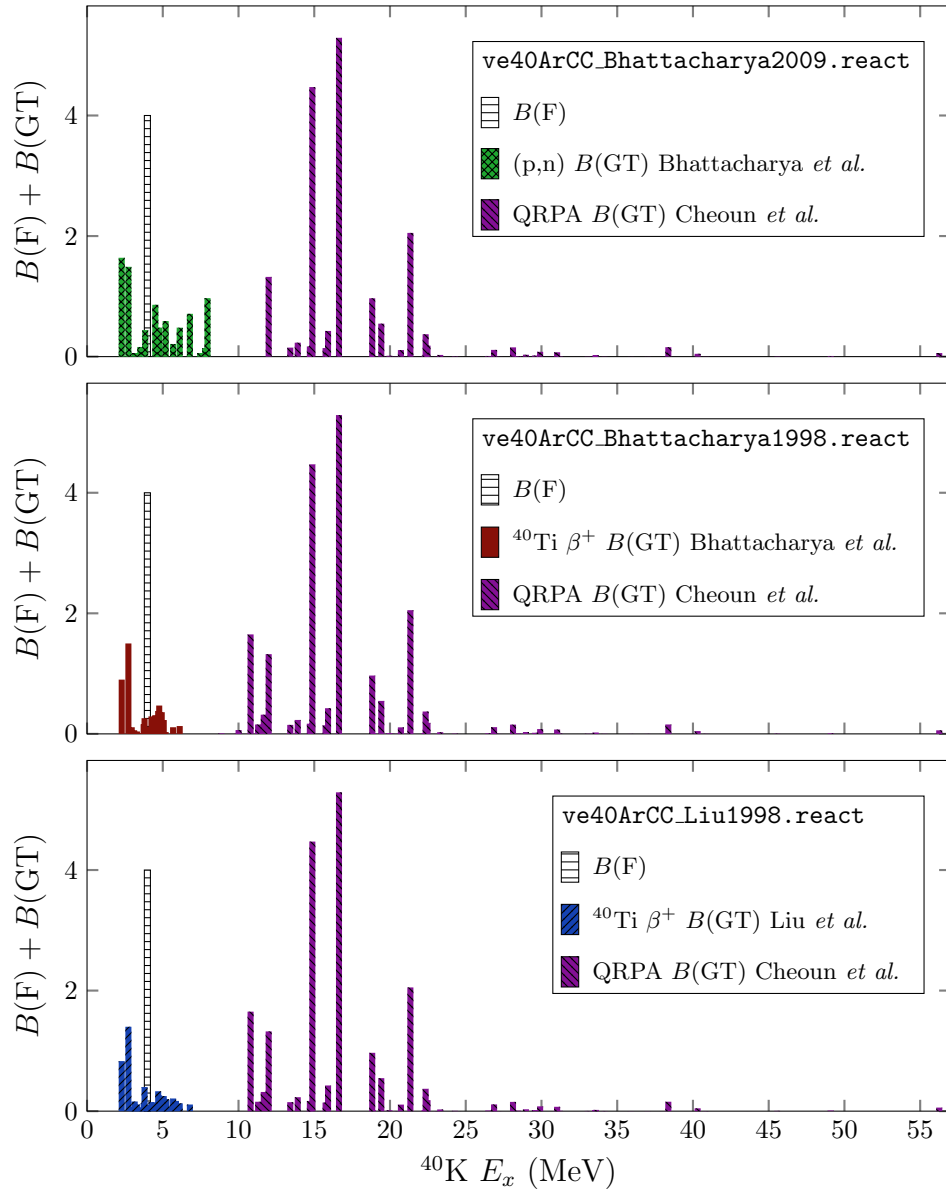


FIG. 3: Complete sets of $^{40}\text{Ar}(\nu_e, e^-)^{40}\text{K}^*$ allowed approximation matrix elements distributed as part of MARLEY 1.2.0. The name of the data file in which each set of matrix elements may be found is given in the appropriate legend heading. The QRPA $B(\text{GT})$ strengths (violet) were calculated by Cheoun *et al.* [69]. Citations for the experimental $B(\text{GT})$ strengths are given in the captions for figs. 1 and 2.

B. Unbound states: statistical emission

The MARLEY approach to modeling de-excitations of unbound nuclear states rests on the assumption of *compound nucleus* formation: the neutrino interaction leaves the nucleus in a state of thermal equilibrium which de-excites independently of the manner in which it was formed. The number of open decay channels is taken to be large enough that competition between them can be modeled statistically. That is, transitions to individual nuclear final states can be neglected in favor of averaging over many states of approximately the same energy

[79]. This last assumption is not strictly true for excitation energies slightly above the lowest fragment emission threshold. In such cases it is adopted as an approximation.

Compound nucleus modeling is a key ingredient in nuclear reaction codes designed to compute nucleon-nucleus and nucleus-nucleus cross sections, such as TALYS, EMPIRE [80], CCONE [81], and CoH₃ [82]. The treatment in MARLEY uses the Hauser-Feshbach formalism [83] common to these other codes.

1. Differential decay widths

For the present application to neutrino-induced de-excitations, the physics content of the Hauser-Feshbach

statistical model (HFSM) may be conveniently summarized by the differential decay widths

$$\frac{d\Gamma_a}{dE'_x} = \frac{1}{2\pi\rho_i(E_x, J, \Pi)} \sum_{\ell=0}^{\infty} \sum_{j=|\ell-s|}^{\ell+s} \sum_{J'=|J-j|}^{J+j} T_{\ell j}(\varepsilon) \rho_f(E'_x, J', \Pi') \quad (38)$$

and

$$\frac{d\Gamma_\gamma}{dE'_x} = \frac{1}{2\pi\rho_i(E_x, J, \Pi)} \sum_{\lambda=1}^{\infty} \sum_{J'=|J-\lambda|}^{J+\lambda} \sum_{\Pi' \in \{-1, 1\}} T_{X\lambda}(E_\gamma) \rho_f(E'_x, J', \Pi'). \quad (39)$$

which describe de-excitations of a compound nuclear state via emission of a fragment a or a γ -ray, respectively.

Here the initial (final) nucleus has excitation energy E_x (E'_x), total spin J (J'), and parity Π (Π'); s , ℓ , and j are the spin, orbital, and total angular momentum quantum numbers of the emitted fragment; ρ_i (ρ_f) is the density of nuclear levels in the vicinity of the initial (final) state; ε is the total kinetic energy of the final particles in the rest frame of the initial nucleus; and E_γ is the energy of the emitted γ -ray. For decays involving emission of a fragment with parity π_a , the value of Π' is fixed by conservation of parity:

$$\Pi' = (-1)^\ell \pi_a \Pi. \quad (40)$$

The possible γ -ray transitions are labeled by their multipolarity $\lambda \geq 1$ and by whether they are *electric* ($X = E$) or *magnetic* ($X = M$) in nature. These two alternatives are distinguished based on the multipolarity and the nuclear parity:

$$X = \begin{cases} E & \Pi = (-1)^\lambda \Pi' \\ M & \Pi = (-1)^{\lambda+1} \Pi' \end{cases}. \quad (41)$$

The transmission coefficients $T_{\ell j}$ and $T_{X\lambda}$ quantify how likely each decay mode is to occur. The methods used to compute them are described in sections IV B 2 and IV B 3. For practical calculations, the infinite sums that appear in eqs. (38) and (39) must be truncated. Because the value of $T_{\ell j}$ ($T_{X\lambda}$) falls off rapidly with increasing ℓ (λ), terms beyond $\ell = \lambda = 5$ are neglected.

The HFSM is often communicated in terms of nuclear scattering cross sections instead of decay widths. To aid the reader in connecting the expressions given here with more standard presentations (see, e.g., refs. [84, 85]), a brief derivation of eq. (38) is provided in appendix A.

2. Fragment transmission coefficients

The fragment transmission coefficients $T_{\ell j}$ used in eq. (38) are computed by solving the radial Schrödinger equation (with relativistic kinematics as recommended in ref. [86])

$$\left[\frac{d^2}{dr^2} + \kappa^2 - \frac{\ell(\ell+1)}{r^2} - \frac{\kappa^2}{\varepsilon} \mathcal{U}(r, \varepsilon_{\text{lab}}, \ell, j) \right] u_{\ell j}(r) = 0 \quad (42)$$

where $u_{\ell j}$ is the fragment's radial wave function,

$$\kappa = \sqrt{\frac{(2m_a + \varepsilon_{\text{lab}}) M'^2 \varepsilon_{\text{lab}}}{(m_a + M')^2 + 2M' \varepsilon_{\text{lab}}}} \quad (43)$$

is the magnitude of its three-momentum in the rest frame of the initial nucleus, and m_a (M') denotes the mass of the emitted fragment (final nucleus). The global nuclear optical potential \mathcal{U} developed by Koning and Delaroche [86] is used in the present calculations. A full description thereof is given in appendix C.

The quantity

$$\varepsilon_{\text{lab}} = \frac{\varepsilon^2 + 2(m_a + M')\varepsilon}{2M'} \quad (44)$$

is the fragment's kinetic energy in the rest frame of the final nucleus. The label *lab* is applied to this variable because it also represents the laboratory-frame kinetic energy for the time-reversed process in which the fragment is absorbed to form the compound nucleus (see appendix A).

The transmission coefficient $T_{\ell j}$ is related to the energy-averaged S-matrix element $\langle S_{\ell j} \rangle$ via

$$T_{\ell j} = 1 - |\langle S_{\ell j} \rangle|^2. \quad (45)$$

The latter quantity may be determined by comparing the

full solution $u_{\ell j}$ of eq. (42) to the asymptotic form

$$u_{\ell j}(r) \rightarrow \frac{i}{2} [H_{\ell}^{-}(\eta, kr) - \langle S_{\ell j} \rangle H_{\ell}^{+}(\eta, kr)] \quad (46)$$

valid for large radii r , where the nuclear optical potential approaches the Coulomb potential. Here H_{ℓ}^{\pm} are the Coulomb wave functions [87, chap. 33]. These depend on the Sommerfeld parameter

$$\eta \equiv \frac{z Z' \alpha}{\beta_{\text{rel}}}, \quad (47)$$

which is evaluated in terms of the proton number z (Z') of the emitted fragment (final nucleus) and the relative speed

$$\beta_{\text{rel}} = \frac{\sqrt{\varepsilon_{\text{lab}}^2 + 2 m_a \varepsilon_{\text{lab}}}}{m_a + \varepsilon_{\text{lab}}}. \quad (48)$$

The numerical techniques used to evaluate the fragment transmission coefficients $T_{\ell j}$ are documented in ref. [48, sec. 2.2.2].

3. Gamma-ray transmission coefficients

The γ -ray transmission coefficients $T_{X\lambda}$ used in eq. (39) may be written in terms of a strength function $f_{X\lambda}(E_{\gamma})$ such that

$$T_{X\lambda}(E_{\gamma}) = 2\pi E_{\gamma}^{2\lambda+1} f_{X\lambda}(E_{\gamma}). \quad (49)$$

To compute γ -ray strength functions in this work, I adopt the Standard Lorentzian model from RIPL-3 [78], which is based on early studies by Brink [88] and Axel [89]. This model assumes that γ -ray emissions of type $X\lambda$ occur via de-excitation of the corresponding giant multipole resonance, which is parameterized in terms of its centroid excitation energy $E_{X\ell}$, width $\Gamma_{X\ell}$, and peak cross section $\sigma_{X\ell}$. The strength function is evaluated according to

$$f_{X\lambda}(E_{\gamma}) = \frac{\sigma_{X\lambda}}{(2\lambda+1)\pi^2} \left[\frac{\Gamma_{X\lambda}^2 E_{\gamma}^{3-2\lambda}}{(E_{\gamma}^2 - E_{X\lambda}^2)^2 + E_{\gamma}^2 \Gamma_{X\lambda}^2} \right] \quad (50)$$

with the values of the giant resonance parameters given in table II. Note that some peak cross sections are given in the table in units of mb while eq. (50) employs natural units.

4. Transitions to discrete nuclear levels

The differential decay widths given in eqs. (38) and (39) are appropriate for use at high excitation energies E'_x where the nuclear levels may be modeled as a continuum. When a discrete level scheme is available for the final-state nuclide, MARLEY uses the excitation energy

of the last tabulated level as the lower bound for the continuum. Otherwise, a continuum level density ρ_f is used all the way down to the ground state ($E'_x = 0$).

Decays to discrete levels of the final-state nucleus are considered by MARLEY in terms of the HFSM partial decay widths

$$\Gamma_a = \frac{1}{2\pi \rho_i(E_x, J, \Pi)} \sum_{j=|J-J'|}^{J+J'} \sum_{\ell=|j-s|}^{j+s} \delta_{\pi}^{\ell} T_{\ell j}(\varepsilon) \quad (51)$$

and

$$\Gamma_{\gamma} = \frac{1}{2\pi \rho_i(E_x, J, \Pi)} \sum_{\lambda=\max(1, |J-J'|)}^{J+J'} T_{X\lambda}(E_{\gamma}). \quad (52)$$

The symbol δ_{π}^{ℓ} , which enforces parity conservation, is equal to one if eq. (40) is satisfied and zero if it is not. If $J + J' < 1$, then the width Γ_{γ} vanishes. The expressions in eqs. (51) and (52) may be derived from eqs. (38) and (39) by treating ρ_f as a delta function centered on the nuclear level of interest.

5. Nuclear level density

In the continuum, the final level density ρ_f is computed according to the Back-shifted Fermi gas model (BFM) described in appendix B. The initial level density ρ_i is evaluated according to the BFM at all excitation energies. However, since the overall factor involving ρ_i cancels out in the evaluation of decay branching ratios, the specific model chosen for ρ_i does not have any impact on the simulation results.

V. RESULTS

In this section, the MARLEY 1.2.0 implementation of the theoretical models described above is used to obtain predictions of total and differential cross sections for the reaction $^{40}\text{Ar}(\nu_e, e^{-})^{40}\text{K}^*$. Because MARLEY calculates the four-momentum of every final-state particle for every event, various additional distributions may be studied beyond those presented in this work.

A. Inclusive cross section

Figure 4 shows MARLEY predictions of the total cross section for inclusive charged-current ν_e absorption on ^{40}Ar . The important role played by the Coulomb corrections discussed in section II B is illustrated by the different curves in the plot. The default MARLEY approach to Coulomb effects, defined in eq. (25), involves choosing the smaller of two correction factors calculated using the Fermi function and using the modified effective momentum approximation (MEMA). In fig. 4, the solid

TABLE II: Giant resonance parameters used herein for γ -ray strength function calculations. Centroid excitation energies $E_{X\lambda}$ and widths $\Gamma_{X\lambda}$ are given in MeV. Peak cross sections for electric multipole resonances ($\sigma_{E\lambda}$) are given in mb, while those for magnetic resonances ($\sigma_{M\lambda}$) are given in MeV^{-2} .

Transition	Parameters
Electric dipole (E1) ^a	$E_{\text{E1}} = 31.2 A^{-1/3} + 20.6 A^{-1/6}$ $\Gamma_{\text{E1}} = 0.026 E_{\text{E1}}^{1.91}$ $\sigma_{\text{E1}} = 1.2 (120 N Z) / (\pi A \Gamma_{\text{E1}})$
Electric quadrupole (E2) ^b	$E_{\text{E2}} = 63 A^{-1/3}$ $\Gamma_{\text{E2}} = 6.11 - 0.012 A$ $\sigma_{\text{E2}} = 0.00014 Z^2 E_{\text{E2}} / (A^{1/3} \Gamma_{\text{E2}})$
Magnetic dipole (M1) ^{c,d}	$E_{\text{M1}} = 41 A^{-1/3}$ $\Gamma_{\text{M1}} = 4$ $\sigma_{\text{M1}} = 3 \pi^2 \left[\frac{(B_n^2 - E_{\text{M1}}^2)^2 + B_n^2 \Gamma_{\text{M1}}^2}{B_n \Gamma_{\text{M1}}^2} \right] \left[\frac{f_{\text{E1}}(B_n)}{0.0588 A^{0.878}} \right]$
Other electric transitions (E λ) ^e	$E_{\text{E}\lambda} = E_{\text{E2}}$ $\Gamma_{\text{E}\lambda} = \Gamma_{\text{E2}}$ $\sigma_{\text{E}\lambda} = (8 \times 10^{-4})^{\lambda-2} \sigma_{\text{E2}}$
Other magnetic transitions (M λ) ^e	$E_{\text{M}\lambda} = E_{\text{M1}}$ $\Gamma_{\text{M}\lambda} = \Gamma_{\text{M1}}$ $\sigma_{\text{M}\lambda} = (8 \times 10^{-4})^{\lambda-1} \sigma_{\text{M1}}$

^a See ref. [90, p. 129]

^b See ref. [91, p. 103]

^c See ref. [90, p. 132]

^d $B_n = 7$ MeV and f_{E1} is calculated using natural units and the E1 parameters above.

^e Default approximation used by version 1.6 of TALYS [76]

black line gives the cross section calculated using the default approach, while the dotted cyan and dashed red lines give, respectively, the corresponding cross sections obtained when the Fermi function and MEMA are used unconditionally. Applying either correction leads to an enhancement of the total cross section over the uncorrected result, which is drawn as the blue dash-dotted line. The relationships between the different approaches to Coulomb corrections in the present calculation are qualitatively similar to those seen previously using a CRPA model [35], but there are some details that are different, e.g., the cross sections calculated using the Fermi function and the MEMA intersect at a neutrino energy between 50–60 MeV, about 10 MeV lower than in the CRPA result.

B. Exclusive cross sections

Figure 5 presents the first calculation at supernova energies of total cross sections for exclusive final states in the reaction $^{40}\text{Ar}(\nu_e, e^-)^{40}\text{K}^*$. Each exclusive channel is labeled in terms of its hadronic content, but zero or more de-excitation γ -rays are allowed even when not explicitly listed. Below a neutrino energy of about 10 MeV, only transitions to bound nuclear levels are energetically possible. These de-excite via γ -ray emission. Single neutron emission becomes appreciable around 15 MeV. Although the proton (7.58 MeV) and alpha particle (6.44 MeV) separation energies for ^{40}K are comparable to the neutron separation energy (7.80 MeV), the Coulomb barrier experienced by these charged particles suppresses their emission relative to neutrons.

Throughout the remainder of this paper, calculations

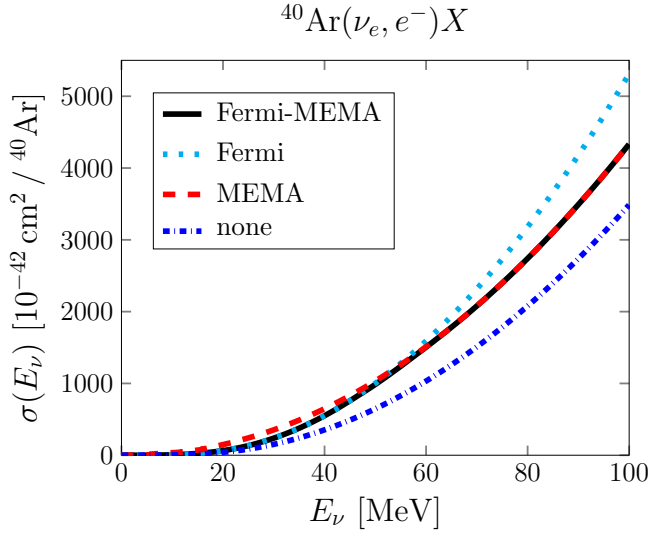


FIG. 4: Inclusive total cross sections for charged-current absorption of ν_e on ^{40}Ar . Each curve shows the result obtained using a specific approach to Coulomb corrections.

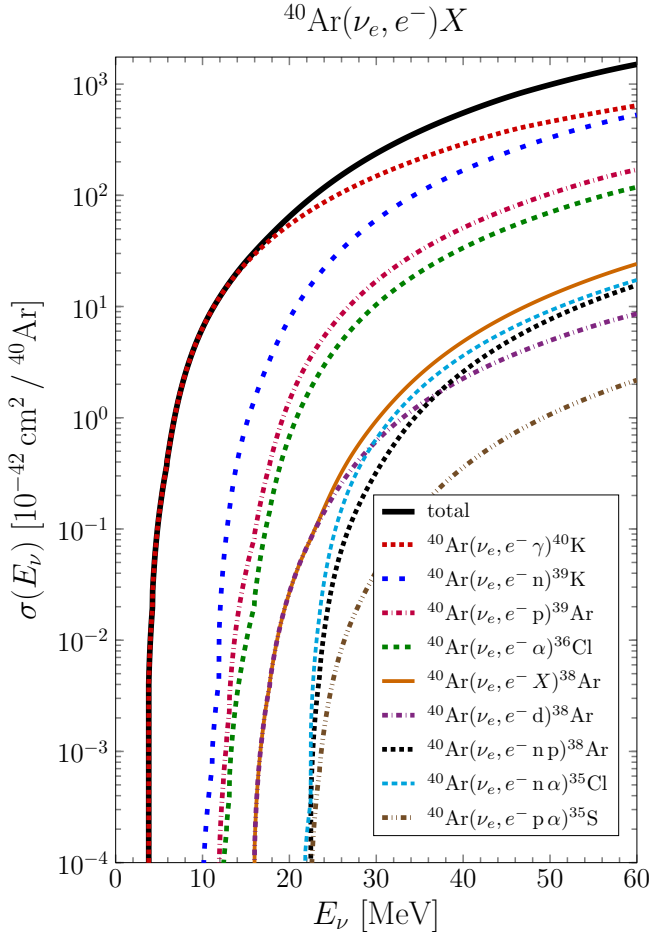


FIG. 5: Exclusive total cross sections for charged-current absorption of ν_e on ^{40}Ar .

TABLE III: Parameters used to compute the supernova neutrino spectrum described in the text. Values of the mean ν_e energy $\langle E_\nu \rangle$ and the elapsed time t are given in MeV and seconds, respectively. The shape parameter α is dimensionless.

Configuration	$\langle E_\nu \rangle$	α	t
SN _T	14.1	2.67	
SN ₁	9	5	0
SN ₂	12	4	0.5
SN ₃	15	3.25	3
SN ₄	17	2.9	6.25

of flux-averaged cross sections will be reported for two distinct sources of low-energy electron neutrinos. The first of these is the approximate supernova neutrino energy spectrum

$$\phi(E_\nu) \propto \left(\frac{E_\nu}{\langle E_\nu \rangle} \right)^\alpha \exp \left[-(\alpha + 1) \frac{E_\nu}{\langle E_\nu \rangle} \right] \quad (53)$$

described in ref. [92]. Here the dependence on the neutrino energy E_ν is expressed in terms of the mean energy $\langle E_\nu \rangle$ and a shape parameter α . Based on an analysis of a simulated supernova, the authors of ref. [92] report values of $\langle E_\nu \rangle = 14.1$ MeV and $\alpha = 2.67$ for the time-integrated ν_e spectrum, which I denote by SN_T. I also consider four instantaneous spectra estimated using fig. 1 of ref. [92]. These are labeled SN₁ through SN₄ in chronological order. Table III gives the values of the spectral parameters and the approximate elapsed time since the start of the supernova for each of these configurations.

The second source of low-energy electron neutrinos considered in this work is the decay

$$\mu^+ \rightarrow e^+ + \nu_e + \bar{\nu}_\mu. \quad (54)$$

For an antimuon decaying at rest (μDAR), the ν_e energy spectrum is given by [93]

$$\phi(E_\nu) \propto E_\nu^2 m_\mu^{-4} (m_\mu - 2E_\nu), \quad (55)$$

where m_μ is the muon mass and the neutrino energy E_ν satisfies

$$0 < E_\nu < m_\mu/2. \quad (56)$$

Experimental facilities which generate large numbers of stopped muons, such as the Spallation Neutron Source at Oak Ridge National Laboratory, provide a valuable opportunity to study tens-of-MeV neutrino interactions using a terrestrial source [94].

Table IV reports a wide variety of flux-averaged total cross sections for each of the electron neutrino spectra $\phi(E_\nu)$ described above. For each entry in the table, the flux-averaged total cross section $\langle \sigma \rangle_f$ for a specific final

state f was obtained via the expression

$$\langle \sigma \rangle_f = \frac{1}{\Phi} \int \phi(E_\nu) \left[\sum_L \sigma_L(E_\nu) R_L(f) \right] dE_\nu \quad (57)$$

where

$$\Phi \equiv \int \phi(E_\nu) dE_\nu \quad (58)$$

and the integrals in eqs. (57) and (58) are over the entire neutrino spectrum. Here σ_L is the inclusive total cross section for transitions to a particular ^{40}K nuclear level L and $R_L(f)$ is the branching ratio for the final state f when the de-excitation cascade begins at the level L . The sum in eq. (57) runs over all energetically-accessible nuclear levels. All quantities in eq. (57) are calculated analytically except for $R_L(f)$, which is estimated using Monte Carlo simulations of de-excitations from every nuclear level listed in the MARLEY input file `ve40ArCC_Bhattacharya1998.react`. The statistical uncertainty associated with each entry in table IV never exceeds 10% and is typically much smaller.

C. Electron angle and energy distributions

Figure 6 shows flux-averaged differential cross sections predicted by MARLEY for the laboratory-frame scattering cosine of the outgoing electron. The upper panel shows the total result (solid black) for the SN_T ν_e spectrum together with the separate contributions arising from Fermi (dashed blue) and Gamow-Teller (dotted red) transitions. The lower panel presents the same quantities for the μDAR ν_e spectrum. Competition between the two linear components of the cross section gives rise to a total angular distribution that is nearly flat in both cases, with SN_T being slightly forward and μDAR slightly backward.

A recent theoretical study [36] has pointed out that forbidden nuclear transitions, which are neglected in the present calculation, have an increasingly strong effect on the electron angular distribution as the neutrino energy grows beyond a few tens of MeV. Deviations from the linear behavior shown in fig. 6 signal the breakdown of the allowed approximation used by MARLEY. A future measurement of the $^{40}\text{Ar}(\nu_e, e^-)^{40}\text{K}^*$ angular differential cross section will thus provide a powerful constraint on the nuclear modeling needed to predict the relative contributions of the allowed and forbidden transitions.

Figure 7 shows the flux-averaged differential cross section with respect to the kinetic energy of the outgoing electron. The inclusive prediction for the SN_T (μDAR) spectrum is shown by the solid black line in the upper (lower) panel, with the other line styles used to represent individual contributions from four exclusive final states. While the cross sections for both spectra are dominated by de-excitation modes involving only γ -rays (loosely dotted blue) or single neutron emission (densely

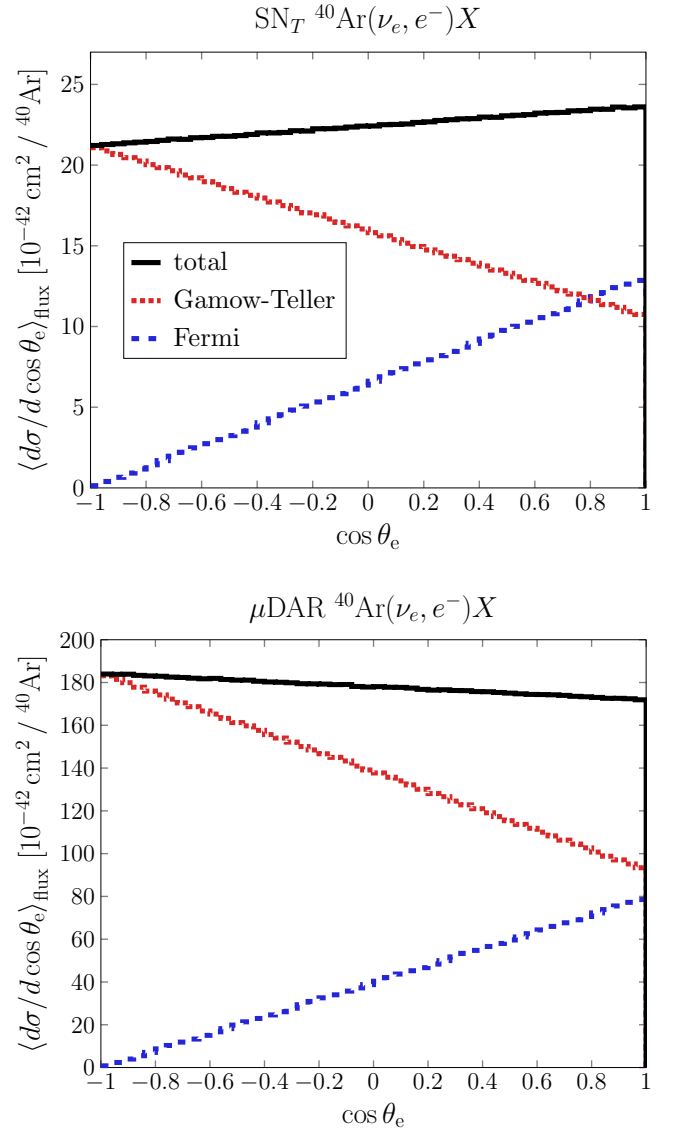


FIG. 6: Flux-averaged differential cross sections with respect to the laboratory-frame scattering cosine $\cos \theta_e$ of the final-state electron. Top: Calculation for the time-integrated supernova ν_e spectrum described in the text. Bottom: Calculation for ν_e produced by μ^+ decay at rest.

dotted red), the contribution of the latter is much more pronounced for the μDAR case. The small cross sections for single proton and single α emission are also noticeably enhanced as one moves from the SN_T spectrum to the μDAR spectrum.

D. Neutrino energy reconstruction

The energy of the incident neutrino is distributed among the final products of the $^{40}\text{Ar}(\nu_e, e^-)^{40}\text{K}^*$ reac-

TABLE IV: Flux-averaged total cross sections computed for several different ν_e spectra described in the text. All numerical values are given in $10^{-42} \text{ cm}^2 / {}^{40}\text{Ar}$. For example, a table entry of 4.5×10^1 should be interpreted as $4.5 \times 10^{-41} \text{ cm}^2 / {}^{40}\text{Ar}$.

Channel	SN_T	μDAR	SN_1	SN_2	SN_3	SN_4
${}^{40}\text{Ar}(\nu_e, e^-)X$	4.5×10^1	3.6×10^2	7.7×10^0	2.2×10^1	5.0×10^1	7.7×10^1
${}^{40}\text{Ar}(\nu_e, e^- \gamma) {}^{40}\text{K}$	3.3×10^1	1.9×10^2	7.3×10^0	1.9×10^1	3.7×10^1	5.2×10^1
${}^{40}\text{Ar}(\nu_e, e^- n) {}^{39}\text{K}$	8.2×10^0	1.0×10^2	3.1×10^{-1}	2.6×10^0	9.2×10^0	1.7×10^1
${}^{40}\text{Ar}(\nu_e, e^- p) {}^{39}\text{Ar}$	2.2×10^0	3.1×10^1	4.9×10^{-2}	5.8×10^{-1}	2.4×10^0	4.6×10^0
${}^{40}\text{Ar}(\nu_e, e^- d) {}^{38}\text{Ar}$	7.8×10^{-2}	1.4×10^0	1.0×10^{-3}	1.7×10^{-2}	8.6×10^{-2}	1.8×10^{-1}
${}^{40}\text{Ar}(\nu_e, e^- t) {}^{37}\text{Ar}$	9.7×10^{-4}	2.3×10^{-2}	3.4×10^{-6}	1.4×10^{-4}	1.1×10^{-3}	2.5×10^{-3}
${}^{40}\text{Ar}(\nu_e, e^- h) {}^{37}\text{Cl}$	7.2×10^{-5}	1.9×10^{-3}	2.0×10^{-7}	9.6×10^{-6}	7.8×10^{-5}	1.9×10^{-4}
${}^{40}\text{Ar}(\nu_e, e^- \alpha) {}^{36}\text{Cl}$	1.3×10^0	2.1×10^1	2.4×10^{-2}	3.2×10^{-1}	1.5×10^0	2.9×10^0
${}^{40}\text{Ar}(\nu_e, e^- n p) {}^{38}\text{Ar}$	5.8×10^{-2}	1.6×10^0	1.4×10^{-4}	7.1×10^{-3}	6.3×10^{-2}	1.6×10^{-1}
${}^{40}\text{Ar}(\nu_e, e^- n d) {}^{37}\text{Cl}$	4.1×10^{-5}	1.7×10^{-3}	6.9×10^{-9}	1.9×10^{-6}	4.1×10^{-5}	1.5×10^{-4}
${}^{40}\text{Ar}(\nu_e, e^- n \alpha) {}^{35}\text{Cl}$	9.0×10^{-2}	2.2×10^0	2.9×10^{-4}	1.3×10^{-2}	9.8×10^{-2}	2.3×10^{-1}
${}^{40}\text{Ar}(\nu_e, e^- p \alpha) {}^{35}\text{S}$	7.9×10^{-3}	2.2×10^{-1}	1.8×10^{-5}	9.4×10^{-4}	8.5×10^{-3}	2.2×10^{-2}
${}^{40}\text{Ar}(\nu_e, e^- 2n p) {}^{37}\text{Ar}$	1.5×10^{-4}	6.7×10^{-3}	2.7×10^{-9}	3.8×10^{-6}	1.5×10^{-4}	6.3×10^{-4}
${}^{40}\text{Ar}(\nu_e, e^- 2\alpha) {}^{32}\text{Si}$	6.4×10^{-4}	2.3×10^{-2}	3.4×10^{-7}	4.7×10^{-5}	6.7×10^{-4}	2.0×10^{-3}
${}^{40}\text{Ar}(\nu_e, e^- 2n) {}^{38}\text{K}$	9.2×10^{-4}	3.6×10^{-2}	2.8×10^{-7}	5.8×10^{-5}	9.5×10^{-4}	3.0×10^{-3}
${}^{40}\text{Ar}(\nu_e, e^- n 2p) {}^{37}\text{Cl}$	2.1×10^{-4}	9.1×10^{-3}	4.6×10^{-9}	5.4×10^{-6}	2.0×10^{-4}	8.4×10^{-4}
${}^{40}\text{Ar}(\nu_e, e^- 2p) {}^{38}\text{Cl}$	6.4×10^{-4}	2.4×10^{-2}	3.3×10^{-7}	4.6×10^{-5}	6.7×10^{-4}	2.0×10^{-3}
${}^{40}\text{Ar}(\nu_e, e^- 3n) {}^{37}\text{K}$	4.2×10^{-6}	1.8×10^{-4}	6.2×10^{-11}	9.8×10^{-8}	4.0×10^{-6}	1.7×10^{-5}
${}^{40}\text{Ar}(\nu_e, e^- 3p) {}^{37}\text{S}$	3.6×10^{-7}	1.5×10^{-5}	4.7×10^{-12}	8.0×10^{-9}	3.5×10^{-7}	1.5×10^{-6}
${}^{40}\text{Ar}(\nu_e, e^- X) {}^{28}\text{Al}$	2.2×10^{-8}	6.6×10^{-7}	1.8×10^{-13}	4.0×10^{-10}	2.1×10^{-8}	9.8×10^{-8}
${}^{40}\text{Ar}(\nu_e, e^- X) {}^{30}\text{P}$	2.6×10^{-9}	2.9×10^{-9}	1.1×10^{-15}	2.0×10^{-11}	2.3×10^{-9}	1.3×10^{-8}
${}^{40}\text{Ar}(\nu_e, e^- X) {}^{30}\text{Si}$	1.5×10^{-7}	3.2×10^{-6}	8.6×10^{-13}	2.3×10^{-9}	1.4×10^{-7}	7.1×10^{-7}
${}^{40}\text{Ar}(\nu_e, e^- X) {}^{31}\text{P}$	4.3×10^{-5}	1.9×10^{-3}	8.7×10^{-10}	1.1×10^{-6}	4.2×10^{-5}	1.7×10^{-4}
${}^{40}\text{Ar}(\nu_e, e^- X) {}^{31}\text{Si}$	3.1×10^{-6}	1.3×10^{-4}	4.6×10^{-11}	7.2×10^{-8}	3.0×10^{-6}	1.3×10^{-5}
${}^{40}\text{Ar}(\nu_e, e^- X) {}^{32}\text{P}$	6.4×10^{-4}	2.3×10^{-2}	3.4×10^{-7}	4.7×10^{-5}	6.7×10^{-4}	2.0×10^{-3}
${}^{40}\text{Ar}(\nu_e, e^- X) {}^{33}\text{P}$	2.6×10^{-7}	8.5×10^{-6}	3.1×10^{-12}	5.2×10^{-9}	2.5×10^{-7}	1.1×10^{-6}
${}^{40}\text{Ar}(\nu_e, e^- X) {}^{33}\text{S}$	2.8×10^{-6}	1.0×10^{-4}	5.9×10^{-11}	6.5×10^{-8}	2.7×10^{-6}	1.2×10^{-5}
${}^{40}\text{Ar}(\nu_e, e^- X) {}^{34}\text{Cl}$	2.8×10^{-5}	1.2×10^{-3}	4.2×10^{-10}	6.6×10^{-7}	2.7×10^{-5}	1.1×10^{-4}
${}^{40}\text{Ar}(\nu_e, e^- X) {}^{34}\text{P}$	1.4×10^{-6}	5.6×10^{-5}	1.9×10^{-11}	3.1×10^{-8}	1.3×10^{-6}	5.6×10^{-6}
${}^{40}\text{Ar}(\nu_e, e^- X) {}^{34}\text{S}$	3.4×10^{-4}	1.5×10^{-2}	1.2×10^{-8}	9.6×10^{-6}	3.3×10^{-4}	1.3×10^{-3}
${}^{40}\text{Ar}(\nu_e, e^- X) {}^{35}\text{Cl}$	9.0×10^{-2}	2.2×10^0	2.9×10^{-4}	1.3×10^{-2}	9.8×10^{-2}	2.3×10^{-1}
${}^{40}\text{Ar}(\nu_e, e^- X) {}^{35}\text{S}$	7.9×10^{-3}	2.2×10^{-1}	1.8×10^{-5}	9.4×10^{-4}	8.5×10^{-3}	2.2×10^{-2}
${}^{40}\text{Ar}(\nu_e, e^- X) {}^{36}\text{Ar}$	1.3×10^{-5}	5.3×10^{-4}	6.8×10^{-10}	3.9×10^{-7}	1.3×10^{-5}	5.2×10^{-5}
${}^{40}\text{Ar}(\nu_e, e^- X) {}^{36}\text{Cl}$	1.3×10^0	2.1×10^1	2.4×10^{-2}	3.2×10^{-1}	1.5×10^0	2.9×10^0
${}^{40}\text{Ar}(\nu_e, e^- X) {}^{36}\text{S}$	5.3×10^{-7}	2.0×10^{-5}	9.5×10^{-12}	1.2×10^{-8}	5.1×10^{-7}	2.2×10^{-6}
${}^{40}\text{Ar}(\nu_e, e^- X) {}^{37}\text{Ar}$	1.2×10^{-3}	3.2×10^{-2}	3.4×10^{-6}	1.5×10^{-4}	1.3×10^{-3}	3.3×10^{-3}
${}^{40}\text{Ar}(\nu_e, e^- X) {}^{37}\text{Cl}$	3.0×10^{-4}	1.2×10^{-2}	2.1×10^{-7}	1.6×10^{-5}	3.0×10^{-4}	1.1×10^{-3}
${}^{40}\text{Ar}(\nu_e, e^- X) {}^{38}\text{Ar}$	1.4×10^{-1}	3.0×10^0	1.2×10^{-3}	2.4×10^{-2}	1.5×10^{-1}	3.4×10^{-1}

tion according to the relation

$$E_\nu = E_{\text{bind}} + E_e + \mathcal{T}_\gamma + \mathcal{T}_{\text{ch}} + \mathcal{T}_n, \quad (59)$$

where E_e is the total energy of the outgoing electron and \mathcal{T}_γ , \mathcal{T}_{ch} , and \mathcal{T}_n are, respectively, the total kinetic energies of all de-excitation γ -rays, charged hadrons, and neutrons in the final state. The small recoil kinetic energy

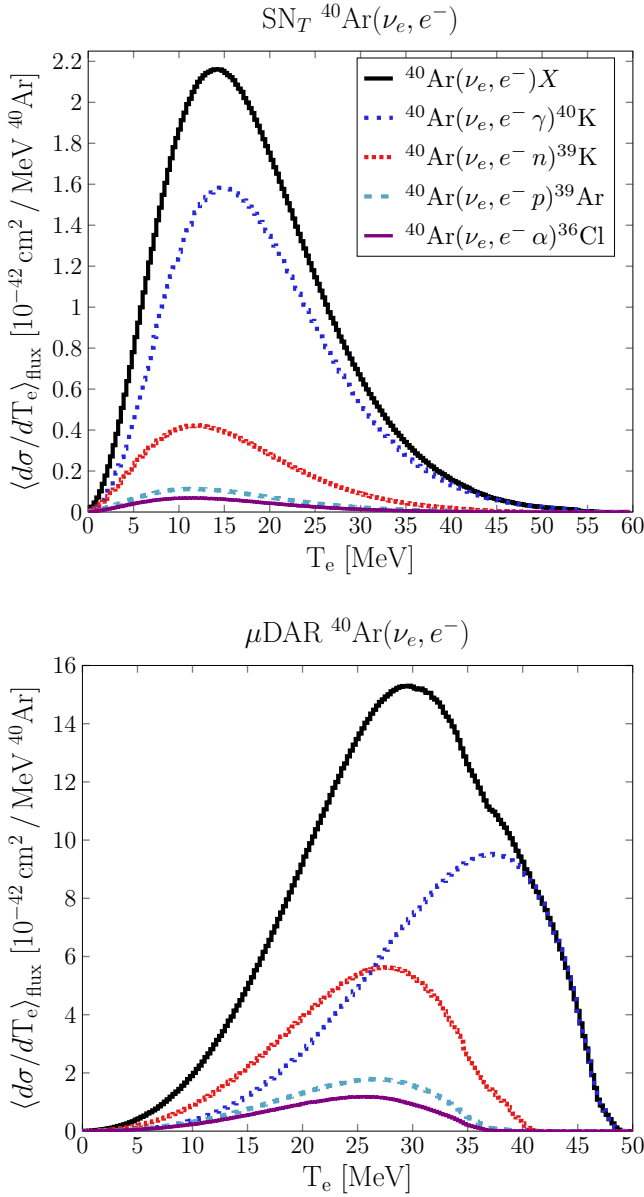


FIG. 7: Flux-averaged differential cross sections with respect to the final-state electron kinetic energy T_e . Top: Calculation for the time-integrated supernova ν_e spectrum described in the text. Bottom: Calculation for ν_e produced by μ^+ decay at rest.

of the remnant nucleus is included in \mathcal{T}_{ch} . The change in binding energy E_{bind} is given by the expression

$$E_{\text{bind}} = \Delta_{\text{RT}} - m_e + \sum_k m_k + \sum_k Q_k m_e \quad (60)$$

if electron binding energies are neglected. Here

$$\Delta_{\text{RT}} \equiv m_{\text{atom}}(\text{R}) - m_{\text{atom}}(\text{T}) \quad (61)$$

is the difference of ground-state atomic masses between the remnant nucleus (R) and the nuclear target (T =

^{40}Ar), m_e is the electron mass, and m_k (Q_k) is the mass (electric charge) of the k th nuclear de-excitation product. The sums in eq. (60) run over all particles emitted during nuclear de-excitations.

The minimum possible change in binding energy,

$$E_{\text{bind}}^{\text{min}} \equiv m_{\text{atom}}(\text{F}) - m_{\text{atom}}(\text{T}) - m_e \quad (62)$$

$$= m_{\text{atom}}(^{40}\text{K}) - m_{\text{atom}}(^{40}\text{Ar}) - m_e = 0.99 \text{ MeV} \quad (63)$$

occurs for final states in which only γ -rays are emitted during nuclear de-excitations. In this case, the nuclide $\text{F} = ^{40}\text{K}$ produced immediately after the primary neutrino interaction and the nuclide R remaining after de-excitations are identical.

Since an a priori correction for $E_{\text{bind}}^{\text{min}}$ may be applied when reconstructing the neutrino energy for any $^{40}\text{Ar}(\nu_e, e^-)^{40}\text{K}^*$ event, eq. (59) may be usefully rewritten in the form

$$E_\nu = E_{\text{bind}}^{\text{min}} + \epsilon_{\text{bind}} + E_e + \mathcal{T}_\gamma + \mathcal{T}_{\text{ch}} + \mathcal{T}_n. \quad (64)$$

Here I have defined the *excess binding energy*

$$\epsilon_{\text{bind}} \equiv E_{\text{bind}} - E_{\text{bind}}^{\text{min}}. \quad (65)$$

For $^{40}\text{K}^*$ de-excitation modes involving only γ -rays (γ), single neutron emission (1n), single proton emission (1p), or the emission of both a single neutron and a single proton (1n1p), the excess binding energy takes the values

$$\epsilon_{\text{bind}}^\gamma = 0 \quad (66)$$

$$\epsilon_{\text{bind}}^{1n} = 7.80 \text{ MeV} \quad (67)$$

$$\epsilon_{\text{bind}}^{1p} = 7.58 \text{ MeV} \quad (68)$$

$$\epsilon_{\text{bind}}^{1n1p} = 14.18 \text{ MeV}. \quad (69)$$

A useful property of the excess binding energy is that only a few discrete values of this variable are likely to occur at supernova energies. A future analysis of supernova neutrino data may therefore attempt to correct for nonzero values of ϵ_{bind} by tagging events in which a nucleon or a heavy fragment was emitted from the struck nucleus.

Beyond the binding energy contributions, the other terms in eq. (64) vary in the degree to which they may be reconstructed by a detector. In a liquid argon time projection chamber (LAR-TPC), the primary electron will produce a cm-scale ionization track which may be used to determine its energy and direction. De-excitation γ -rays will produce isolated small energy depositions within several tens of cm of the interaction vertex, primarily via Compton scattering on atomic electrons. Reconstruction of both of these features for supernova neutrino interactions is considered in ref. [31], with the conclusion that the energy associated with each can largely be recovered

under realistic detector performance assumptions. Neutron tagging and calorimetry, on the other hand, were found to be far more challenging.

Low-energy charged nuclear fragments, such as protons and alpha particles, may also produce observable ionizations in a LArTPC. A key challenge for identifying the activity induced by these particles is that, at the energies relevant for supernova neutrinos, charged hadrons will produce mm-scale or smaller ionization tracks. These will likely be difficult to distinguish from the longer track produced by the primary electron. However, if events involving charged nuclear fragment emission can be successfully tagged, perhaps by identifying unusually large charge deposits near the start of the primary electron track, then at least some of the charged hadron kinetic energy may be recoverable.

To assess the relative importance of the various terms on the right-hand side of eq. (64), I define several observables, all of which may be interpreted as a reconstructed neutrino energy E_ν^{reco} under different, often quite optimistic, assumptions. The simplest reconstruction method involves adding the outgoing electron's total energy to the minimum possible change in binding energy for CC ν_e absorption on ^{40}Ar :

$$E_e^{\text{reco}} \equiv E_{\text{bind}}^{\text{min}} + E_e. \quad (70)$$

This estimate of the neutrino energy may be refined by adding the summed energies of all de-excitation γ -rays

$$E_{e+\gamma}^{\text{reco}} \equiv E_e^{\text{reco}} + \mathcal{T}_\gamma \quad (71)$$

and further refined by adding the summed kinetic energies of all final-state charged hadrons

$$E_{\text{vis}}^{\text{reco}} \equiv E_{e+\gamma}^{\text{reco}} + \mathcal{T}_{\text{ch}}. \quad (72)$$

I call the last of these variables the *visible energy* while recognizing that low-energy neutrons may nevertheless produce some observable signals in a LArTPC.

Finally, I consider three possible strategies for implementing a binding energy correction via tagging of final-state nuclear fragments. All three involve conditionally adding one or more terms to the expression for the visible energy above. Under the assumption that de-excitation neutrons may be successfully tagged, I define the reconstructed neutrino energy

$$E_{\text{tag}}^{\text{n}} \equiv E_{\text{vis}}^{\text{reco}} + \delta_{\text{n}} \epsilon_{\text{bind}}^{\text{1n}} \quad (73)$$

in which the symbol δ_{n} is defined to be unity when a MARLEY event contains at least one final-state neutron and zero otherwise. Similarly, under the assumption that charged nuclear fragment emission may be successfully identified, I define

$$E_{\text{tag}}^{\text{p}} \equiv E_{\text{vis}}^{\text{reco}} + \delta_{\text{ch}} \epsilon_{\text{bind}}^{\text{1p}} \quad (74)$$

in which δ_{ch} is unity when a MARLEY event contains a

charged nuclear fragment in the final state and zero when it does not. In an ideal scenario in which both of these tagging techniques are reliable, a still more refined estimate of the neutrino energy may be obtained via

$$E_{\text{tag}}^{\text{n+p}} \equiv E_{\text{vis}}^{\text{reco}} + \delta_{\text{n}} (1 - \delta_{\text{ch}}) \epsilon_{\text{bind}}^{\text{1n}} + \delta_{\text{ch}} (1 - \delta_{\text{n}}) \epsilon_{\text{bind}}^{\text{1p}} + \delta_{\text{n}} \delta_{\text{ch}} \epsilon_{\text{bind}}^{\text{1n1p}}. \quad (75)$$

Figure 8 shows the MARLEY prediction for flux-averaged differential sections with respect to each of these observables. The top (bottom) panel of the figure presents results for the SN_T (μDAR) energy spectrum defined earlier. A solid black line is used to draw the differential cross section with respect to the true neutrino energy, while the other line styles represent the various methods for reconstructing it. The $E_{\text{vis}}^{\text{reco}}$ result is not shown in the top panel since it is difficult to distinguish from the $E_{e+\gamma}^{\text{reco}}$ one on the scale of the plot.

For both spectra studied, the agreement between the reconstructed and true neutrino energy distributions improves most dramatically as one moves from using only the primary electron (E_e^{reco} , thin dashed green) to using both the electron and the de-excitation γ -rays ($E_{e+\gamma}^{\text{reco}}$, densely dotted brown) in the reconstruction. Although inclusion of information about charged hadrons is also seen to be helpful, the next most important improvement comes from the inclusion of binding energy corrections related to neutron tagging ($E_{\text{tag}}^{\text{n}}$, thick dashed violet). Due to the higher mean energy of the μDAR spectrum, nuclear fragment emission becomes more important relative to SN_T , and the impact of the tagging-based binding energy corrections on neutrino energy reconstruction becomes more pronounced.

To further quantify the performance of each of these energy reconstruction methods, fig. 9 reports the fractional root mean square (RMS) resolution

$$f_{\text{RMS}}(E_\nu) \equiv \sqrt{\left\langle \left(\frac{E_\nu^{\text{reco}} - E_\nu}{E_\nu} \right)^2 \right\rangle} \quad (76)$$

for each definition of the reconstructed neutrino energy E_ν^{reco} above. Here, the angle brackets denote the arithmetic mean of the enclosed quantity. The choice of f_{RMS} as a metric is intended to facilitate comparisons with fig. 4 of ref. [31] and fig. 7 of ref. [15], both of which use the same quantity to study energy reconstruction in a full LArTPC detector simulation. The results are shown in small bins of the true neutrino energy E_ν . To obtain the curves shown in fig. 9, a large sample of MARLEY events was generated, and a Monte Carlo estimator for f_{RMS} was evaluated via

$$f_{\text{RMS}}(E_\nu \in b) \approx \sqrt{\frac{1}{N_b} \sum_{j=1}^{N_b} \left[\frac{E_\nu^{\text{reco}}(j) - E_\nu(j)}{E_\nu(j)} \right]^2} \quad (77)$$

where the sum runs over over the N_b simulated events

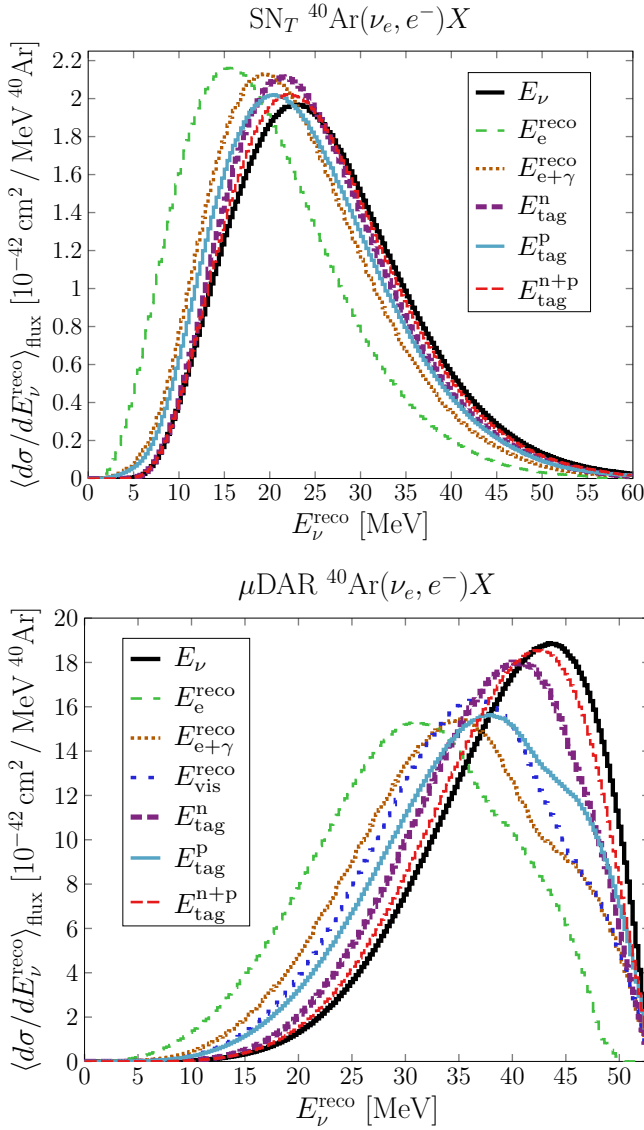


FIG. 8: Flux-averaged differential cross sections with respect to various definitions of the reconstructed neutrino energy E_ν^{reco} . Top: Calculation for the time-integrated supernova ν_e spectrum described in the text. Bottom: Calculation for ν_e produced by μ^+ decay at rest.

which fell into the neutrino energy bin b of interest.

The vertical line seen around 4 MeV for the E_e^{reco} curve (thin dashed green) corresponds to the **MARLEY** energy threshold for CC ν_e absorption. Because the third-forbidden transition between the ground states of ^{40}Ar ($J^\pi = 0^+$) and ^{40}K ($J^\pi = 4^-$) is neglected under the allowed approximation, **MARLEY** predicts a finite resolution for E_e^{reco} even at threshold.

The considerable improvements in energy resolution seen between E_e^{reco} and $E_{e+\gamma}^{\text{reco}}$ (densely dotted brown) and between $E_{e+\gamma}^{\text{reco}}$ and $E_{\text{tag}}^{\text{n}}$ (thick dashed violet) further highlight the conclusions mentioned above with re-

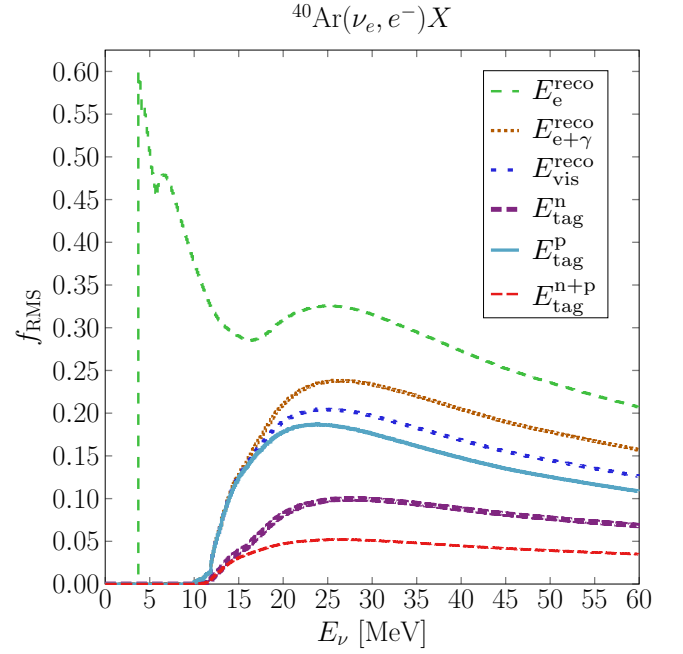


FIG. 9: Fractional RMS resolution for the neutrino energy reconstruction methods described in the text.

spect to fig. 8: while ν_e energy reconstruction in CC absorption on argon will benefit from increased information about any final-state particle species, determining the de-excitation γ -ray energies and tagging neutrons are both particularly impactful.

VI. SUMMARY AND CONCLUSIONS

Due to the potential for DUNE to obtain a once-in-a-lifetime large-statistics measurement of supernova electron neutrinos, achieving a detailed understanding of tens-of-MeV neutrino-argon interactions is an investment that may yield a high scientific return. This paper expands the ability to model these interactions by providing a first calculation of exclusive cross sections for the $^{40}\text{Ar}(\nu_e, e^-)^{40}\text{K}^*$ reaction at supernova energies. The implementation of the models underlying this calculation in the **MARLEY** event generator enables studies of neutrino energy reconstruction to be carried out easily. The simple approach pursued in section V D reveals the substantial role that measuring the energies of de-excitation γ -rays and (though difficult) neutron tagging may play in optimizing supernova ν_e energy resolution in a future analysis by DUNE. Further insights are available by using **MARLEY** in conjunction with a realistic detector simulation [15, 31].

Two major approximations adopted in **MARLEY** 1.2.0 constitute limitations on the present study that should be revisited in future research. The first of these is the allowed approximation invoked during derivation of the inclusive differential cross section in section II A. In a

more detailed calculation of this cross section, the factor $e^{i\mathbf{q}\cdot\mathbf{x}(n)}$ that appears in the nuclear matrix element from eq. (8) is expanded in a series of multipoles [95] that depend on the spherical Bessel function $j_J(|\mathbf{q}|r_n)$, where r_n is the magnitude of $\mathbf{x}(n)$ and J is the multipole order. Terms representing forbidden nuclear transitions ($J > 0$) vanish in the $|\mathbf{q}| \rightarrow 0$ limit imposed by the allowed approximation, but their contribution to the cross section becomes increasingly important as the momentum transfer grows. Since the centroid energy of the multipole giant resonances grows with J roughly like $41 J A^{-1/3}$ MeV [96], the inclusion of forbidden transitions should enhance neutrino scattering to high-lying unbound nuclear states which de-excite primarily via fragment emission. The degree to which this observation affects the present results may be studied in the future by combining a more detailed calculation of the inclusive differential cross section with the MARLEY de-excitation model.

The second major approximation used in this work, which is shared by nearly all calculations of exclusive cross sections for tens-of-MeV neutrino-nucleus scattering, is the compound nucleus assumption discussed in section IV B. Further investigation, both theoretical and experimental, will be needed to clarify the degree to which direct knock-out and pre-equilibrium processes may safely be neglected in models of low-energy neutrino-nucleus reactions. A key question is how the transition between the compound nucleus picture, which is standard for low-energy neutrinos, and the intranuclear cascade picture, which is commonly used in models of accelerator neutrino interactions, should be handled as a function of neutrino energy.

Although the current discussion has focused specifically on the description of nuclear de-excitations following CC ν_e absorption on ^{40}Ar , the model presented in section IV is sufficiently general that it may be applied unaltered in a variety of other contexts. A natural next step is the use of MARLEY together with an inclusive description of inelastic neutral-current scattering on argon, a process for which de-excitations provide the only experimental observables apart from nuclear recoil. While measurements of tens-of-MeV neutrino-argon inelastic cross sections must be pursued to meet the needs of the DUNE supernova neutrino program, more immediate opportunities for confronting MARLEY with data may become available if the code is used to obtain predictions for other nuclei. Near-future measurements that could provide a detailed test of MARLEY include studies of CC ν_e absorption on carbon by JSNS² [33] and neutrino-induced neutron production on lead, iron, and copper by COHERENT [97]. Measurements of exclusive cross sections and decay rates for processes that are closely related to neutrino interactions, such as electron-nucleus scattering [45] and muon capture [98, 99], may also provide helpful model constraints. Finally, the capabilities of MARLEY may prove useful in simulating nuclear de-excitations induced by processes beyond the Standard Model, including nucleon decay [100, 101] and the ab-

sorption of fermionic dark matter [102, 103].

VII. ACKNOWLEDGEMENTS

I thank Myung-Ki Cheoun for providing the QRPA matrix elements used in this work, and I am grateful to the TALYS authors for the decision to release their nuclear structure data files under the terms of the GNU General Public License.

Robert Svoboda, Ramona Vogt, and Michael Mulhearn provided helpful feedback on the doctoral thesis [34] that was a precursor to this publication.

I gratefully acknowledge financial support while at the University of California, Davis from the John Jungerman-Charles Soderquist Graduate Fellowship and from the DOE National Nuclear Security Administration through the Nuclear Science and Security Consortium under award number DE-NA0003180.

This manuscript has been authored by Fermi Research Alliance, LLC under Contract No. DE-AC02-07CH11359 with the U.S. Department of Energy, Office of Science, Office of High Energy Physics.

The high-statistics MARLEY calculations reported herein were performed using resources provided by the Open Science Grid, which is supported by the National Science Foundation and the U.S. Department of Energy's Office of Science.

Appendix A: Decay width for fragment emission

In this appendix, I give a brief derivation of the expression in eq. (38) for the nuclear fragment emission differential decay width of a compound nucleus. A similar approach can be used to obtain the result in eq. (39) for γ -ray emission. The argument presented here is a modern version of one originally given by Weisskopf in ref. [79].

Consider the decay process $i \rightarrow a + f$ in which a compound nucleus i emits a fragment a to become a final-state nucleus f . Adopt the same notation as in section IV B 1: the initial (final) nucleus has spin J (J'), parity Π (Π'), and mass M (M'). The emitted fragment has spin s , orbital (total) angular momentum ℓ (j), three-momentum magnitude k , mass m_a , and parity π_a . Denote the initial nuclear excitation energy by E_x , and let the final nuclear excitation energy lie on the small interval $[E'_x, E'_x + dE'_x]$. The symbol ρ_i (ρ_f) denotes the spin-parity dependent level density (see appendix B 2) in the vicinity of E_x (E'_x) for the initial (final) nucleus.

Within an arbitrary volume V and in the rest frame of the initial nucleus, the number of states n_{a+f} that may be populated by the decay is given by

$$n_{a+f} = n_a n_f \quad (\text{A1})$$

where

$$n_a = (2s + 1) \frac{V}{2\pi^2} \kappa^2 \left| \frac{d\kappa}{dE'_x} \right| dE'_x \quad (\text{A2})$$

and

$$n_f = (2J' + 1) \rho_f(E'_x, J', \Pi') dE'_x. \quad (\text{A3})$$

By detailed balance, the decay width Γ_{a+f} is related to the width Γ_i of the time-reversed absorption process $a + f \rightarrow i$ via

$$\Gamma_{a+f} = \frac{n_{a+f}}{n_i} \Gamma_i \quad (\text{A4})$$

where

$$n_i = (2J + 1) \rho_i(E_x, J, \Pi) \frac{dE_x}{dE'_x} dE'_x \quad (\text{A5})$$

is the number of states in which the compound nucleus i may be formed. The absorption width may be written as

$$\Gamma_i = \phi \sigma \quad (\text{A6})$$

where

$$\phi = \frac{M \kappa}{V E_a E_f} = \frac{1}{V} \frac{dE_x}{d\kappa} \quad (\text{A7})$$

is the particle flux and

$$\sigma = \frac{\pi (2J + 1)}{\kappa^2 (2s + 1)(2J' + 1)} \sum_{\ell=0}^{\infty} \sum_{j=|\ell-s|}^{\ell+s} T_{\ell j}(\epsilon) \quad (\text{A8})$$

is the compound nucleus formation cross section. Here E_a (E_f) is the total energy of the emitted fragment (final nucleus) and

$$\epsilon = M - m_a - M' \quad (\text{A9})$$

is the total kinetic energy of the $a + f$ system. A derivation of the expression in eq. (A8) is given² in ref. [34]. Similar derivations can also be found in, e.g., refs. [84, 85].

Combining the results above and summing over the allowed values of J' , which satisfies the triangle relation

$$|J - j| \leq J' \leq J + j, \quad (\text{A10})$$

leads immediately to eq. (38).

² Note that there is a misprint in equations (A.5) and (A.6) from ref. [34]. The quantities $\ell \pm s_A$, $\ell' \pm s_B$, and $\ell \pm s_b$ should be replaced wherever they occur with, respectively, $j \pm s_A$, $j' \pm s_B$, and $\ell' \pm s_b$.

Appendix B: Level density model

The nuclear level density model used in the present calculations is the RIPL-3 parameterization [78] of the Back-shifted Fermi gas Model (BFM), which is based on the work of Koning, Hilaire, and Goriely [73]. The “back shift” used by this model, which accounts for nucleon pairing effects, involves replacing the nuclear excitation energy E_x by an effective value U defined by

$$U \equiv E_x - \Delta \quad (\text{B1})$$

where the energy shift

$$\Delta = \chi_{\text{pair}} \frac{12 \text{ MeV}}{\sqrt{A}} + \delta \quad (\text{B2})$$

is adjusted to fit experimental data using the empirical parameter δ . The pairing factor χ_{pair} is defined by

$$\chi_{\text{pair}} \equiv \begin{cases} 1 & \text{even-even} \\ 0 & \text{odd-}A \\ -1 & \text{odd-odd.} \end{cases} \quad (\text{B3})$$

1. Total level density

Under the Back-shifted Fermi gas model (BFM), the total density of nuclear levels near excitation energy E_x is given by the expression [73]

$$\rho(E_x) = \left[\frac{1}{\rho_F(E_x)} + \frac{1}{\rho_0(E_x)} \right]^{-1} \quad (\text{B4})$$

where

$$\rho_F(E_x) \equiv \frac{1}{\sqrt{2\pi}\sigma} \frac{\sqrt{\pi}}{12} \frac{\exp(2\sqrt{a_{\text{LD}} U})}{a_{\text{LD}}^{1/4} U^{5/4}} \quad (\text{B5})$$

is the Fermi gas level density and

$$\rho_0(E_x) = \frac{a_{\text{LD}}}{12\sigma} \exp(a_{\text{LD}} U + 1) \quad (\text{B6})$$

is a correction intended to suppress the unphysical divergence of $\rho_F(E_x)$ at low excitation energies.

Although a constant value for the level density parameter a_{LD} is sometimes used, I adopt the energy-dependent functional form [104] recommended by RIPL-3 to correct for the damping of shell effects at high excitation energies:

$$\begin{aligned} a_{\text{LD}} &\equiv a_{\text{LD}}(E_x, Z, A) \\ &= \tilde{a}(A) \left\{ 1 + \frac{\delta W(Z, A)}{U} [1 - \exp(-\gamma U)] \right\}. \end{aligned} \quad (\text{B7})$$

Here $\delta W(Z, A)$ is the shell correction energy, $\tilde{a}(A)$ is the asymptotic value of a_{LD} at high excitation energies, and

γ is a damping parameter that represents how quickly $a_{\text{LD}}(E_x, Z, A)$ approaches $\tilde{a}(A)$. The values of these three parameters are given by the relations

$$\delta W(Z, A) = \delta M_{\text{exp}}(Z, A) - \delta M_{\text{LDM}}(Z, A) \quad (\text{B8})$$

$$\tilde{a} = \alpha A + \beta A^{2/3} \quad (\text{B9})$$

$$\gamma = \gamma_0 A^{-1/3} \quad (\text{B10})$$

where $\delta M_{\text{exp}}(Z, A)$ is the measured nuclear mass excess [71, 105] for the nuclide with proton number Z and mass number A , and $\delta M_{\text{LDM}}(Z, A)$ is the corresponding prediction for the nuclear mass excess using the liquid drop model [78, p. 3164] [72, 106].

This work uses the global “BFM effective” values of the empirical parameters α , β , δ , and γ_0 obtained in ref. [73] using fits to nuclear level data:

$$\alpha = 0.072\,239\,6 \text{ MeV}^{-1} \quad \beta = 0.195\,267 \text{ MeV}^{-1} \quad (\text{B11})$$

$$\gamma_0 = 0.410\,289 \text{ MeV}^{-1} \quad \delta = 0.173\,015 \text{ MeV}. \quad (\text{B12})$$

2. Spin dependence

The density of nuclear levels $\rho(E_x, J, \Pi)$ with total spin J and parity Π near excitation energy E_x may be written in the form

$$\rho(E_x, J, \Pi) = \pi(E_x, J, \Pi) R(E_x, J) \rho(E_x) \quad (\text{B13})$$

where $R(E_x, J)$ is the nuclear spin distribution and $\pi(E_x, J, \Pi)$ is the parity distribution.

Under the assumption that the individual nucleon spins are pointing in random directions, it can be shown [107] that the spin distribution $R(E_x, J)$ is given by [73]

$$R(E_x, J) = \frac{2J+1}{2\sigma^2} \exp \left[-\frac{(J + \frac{1}{2})^2}{2\sigma^2} \right]. \quad (\text{B14})$$

The spin cutoff parameter σ determines the width of $R(E_x, J)$. To calculate this parameter, I adopt the expression recommended by RIPL-3 [78] in the absence of discrete level data:

$$\begin{aligned} \sigma^2 &= \sigma^2(E_x) \\ &= \begin{cases} \sigma_{d,\text{global}}^2 + \frac{E_x}{S_n} \left[\sigma_F^2(S_n) - \sigma_{d,\text{global}}^2 \right] & \text{for } E_x < S_n \\ \sigma_F^2(E_x) & \text{for } E_x \geq S_n. \end{cases} \end{aligned} \quad (\text{B15})$$

Here S_n is the neutron separation energy,

$$\sigma_F^2(E_x) \equiv (0.013\,89 \text{ MeV}^{-1}) \frac{A^{5/3}}{\tilde{a}} \sqrt{a_{\text{LD}} U}, \quad (\text{B16})$$

and

$$\sigma_{d,\text{global}} \equiv 0.83 A^{0.26}. \quad (\text{B17})$$

3. Parity dependence

Most level density calculations assume equipartition of parity, i.e.,

$$\pi(E_x, J, \Pi) = \frac{1}{2}. \quad (\text{B18})$$

I adopt this assumption in agreement with RIPL-3. However, I note that more sophisticated treatments of $\pi(E_x, J, \Pi)$ have been proposed (see, e.g., ref. [108]).

Appendix C: Optical potential

For the statistical model calculations reported here and implemented in MARLEY, the global nuclear optical potential developed by Koning and Delaroche [86] has been adopted. This phenomenological potential is based on fits to nucleon-nucleus scattering data and may be written in the form

$$\mathcal{U} = -\mathcal{V}_V - i\mathcal{W}_V - i\mathcal{W}_D + d_{\ell s} (\mathcal{V}_{SO} + i\mathcal{W}_{SO}) + \mathcal{V}_C. \quad (\text{C1})$$

Here

$$d_{\ell s} \equiv j(j+1) - \ell(\ell+1) - s(s+1). \quad (\text{C2})$$

is the eigenvalue of the spin-orbit operator $2\boldsymbol{\ell} \cdot \mathbf{s}$ for a projectile with definite total angular momentum j , orbital angular momentum ℓ , and spin s .

The Coulomb potential \mathcal{V}_C is taken to be that of a uniformly-charged sphere:

$$\mathcal{V}_C(r) = \begin{cases} \frac{Zze^2}{2R_C} \left(3 - \frac{r^2}{R_C^2} \right) & r < R_C \\ \frac{Zze^2}{r} & r \geq R_C \end{cases} \quad (\text{C3})$$

In the expression above, r is the radial coordinate of the projectile, Z (z) is the proton number of the target nucleus (projectile), e is the elementary charge, and R_C is the Coulomb radius of the nucleus.

1. Nucleon projectiles

The volume (V), surface (D), and spin-orbit (SO) terms of the optical potential are functions that may be expressed as the product of an energy-dependent well

depth and an energy-independent radial part:

$$\mathcal{V}_V = V_V(\varepsilon_{\text{lab}}) f(r, R_V, a_V) \quad (\text{C4})$$

$$\mathcal{W}_V = W_V(\varepsilon_{\text{lab}}) f(r, R_V, a_V) \quad (\text{C5})$$

$$\mathcal{W}_D = -4 a_D^{\mathcal{N}} W_D(\varepsilon_{\text{lab}}) \frac{d}{dr} f(r, R_D, a_D^{\mathcal{N}}) \quad (\text{C6})$$

$$\mathcal{V}_{SO} = V_{SO}(\varepsilon_{\text{lab}}) \frac{1}{m_\pi^2 r} \frac{d}{dr} f(r, R_{SO}, a_{SO}) \quad (\text{C7})$$

$$\mathcal{W}_{SO} = W_{SO}(\varepsilon_{\text{lab}}) \frac{1}{m_\pi^2 r} \frac{d}{dr} f(r, R_{SO}, a_{SO}) \quad (\text{C8})$$

Here m_π is the mass of a charged pion, and the well depths V_V , W_V , etc., are real-valued functions of the laboratory kinetic energy ε_{lab} of the projectile.

The radial dependence in eqs. (C4)–(C8) is given by the Woods-Saxon [109] shape

$$f(r, R, a) = (1 + \exp[(r - R)/a])^{-1} \quad (\text{C9})$$

with effective radius R and diffuseness parameter a . Table V lists the values of the parameters needed to compute the radially-dependent parts of the nuclear optical potential. Each effective radius R_j is related to its tabulated parameter r_j via

$$R_j = r_j A^{1/3} \quad j \in \{V, D, SO, C\}. \quad (\text{C10})$$

Note that all parameter values listed in table V are given in fm, while the expressions given in the text assume natural units ($\hbar = c = 1$).

The expressions for the well depths are most conveniently written in terms of

$$\mathcal{E} \equiv \varepsilon_{\text{lab}} - E_F^{\mathcal{N}}, \quad (\text{C11})$$

the difference between the laboratory-frame kinetic energy of the projectile ε_{lab} and the nuclear Fermi energy $E_F^{\mathcal{N}}$ for the projectile species $\mathcal{N} \in \{p, n\}$ of interest:

$$V_V(\varepsilon_{\text{lab}}) = v_1^{\mathcal{N}} (1 - v_2^{\mathcal{N}} \mathcal{E} + v_3^{\mathcal{N}} \mathcal{E}^2 - v_4^{\mathcal{N}} \mathcal{E}^3) + V_{\text{Coul}} \quad (\text{C12})$$

$$W_V(\varepsilon_{\text{lab}}) = \frac{w_1^{\mathcal{N}} \mathcal{E}^2}{\mathcal{E}^2 + (w_2^{\mathcal{N}})^2} \quad (\text{C13})$$

$$W_D(\varepsilon_{\text{lab}}) = \frac{d_1^{\mathcal{N}} \mathcal{E}^2}{\mathcal{E}^2 + (d_3^{\mathcal{N}})^2} \exp(-d_2^{\mathcal{N}} \mathcal{E}) \quad (\text{C14})$$

$$V_{SO}(\varepsilon_{\text{lab}}) = v_{so1}^{\mathcal{N}} \exp(-v_{so2}^{\mathcal{N}} \mathcal{E}) \quad (\text{C15})$$

$$W_{SO}(\varepsilon_{\text{lab}}) = \frac{w_{so1}^{\mathcal{N}} \mathcal{E}^2}{\mathcal{E}^2 + (w_{so2}^{\mathcal{N}})^2} \quad (\text{C16})$$

TABLE V: Radial parameters for the global nuclear optical potential defined in ref. [86].

Parameter	Value (fm)
r_V	$1.3039 - 0.4054 A^{-1/3}$
a_V	$0.6778 - 1.487 \times 10^{-4} A$
r_D	$1.3424 - 0.01585 A^{1/3}$
a_D^n	$0.5446 - 1.656 \times 10^{-4} A$
a_D^p	$0.5187 + 5.205 \times 10^{-4} A$
r_{SO}	$1.1854 - 0.647 A^{-1/3}$
a_{SO}	0.59
r_C	$1.198 + 0.697 A^{-2/3} + 12.994 A^{-5/3}$

Here the Coulomb contribution to V_V is given by

$$V_{\text{Coul}} \equiv \delta_{p\mathcal{N}} \bar{V}_C v_1^p (v_2^p - 2 v_3^p \mathcal{E} + 3 v_4^p \mathcal{E}^2) \quad (\text{C17})$$

where the symbol $\delta_{p\mathcal{N}}$ is defined by

$$\delta_{p\mathcal{N}} \equiv \begin{cases} 0 & \mathcal{N} = n \\ 1 & \mathcal{N} = p. \end{cases} \quad (\text{C18})$$

Tables 10 and 11 from ref. [86] list the parameters needed to calculate the well depths for a nucleon projectile.

2. Complex projectiles

To compute the nuclear optical potential for complex projectiles ($A > 1$), **MARLEY** implements a superposition model based on a recommendation by Madland [110]. It is equivalent to the default treatment used by **TALYS**. Under this approach, the radial optical model parameters for a projectile with mass number A and proton (neutron) number Z (N) are computed by weighting the corresponding parameters for individual nucleons:

$$r_V = \frac{N r_V^n + Z r_V^p}{A} \quad r_D, r_{SO} \text{ likewise} \quad (\text{C19})$$

$$a_V = \frac{N a_V^n + Z a_V^p}{A} \quad a_D, a_{SO} \text{ likewise.} \quad (\text{C20})$$

The Coulomb radius parameter r_C remains unchanged from the nucleon case. The well depths are evaluated

according to the relations

$$V_V(\varepsilon_{\text{lab}}) = N V_V^n(\varepsilon_{\text{lab}}/A) + Z V_V^p(\varepsilon_{\text{lab}}/A) \quad (\text{C21})$$

W_V, W_D likewise

$$V_{SO}(\varepsilon_{\text{lab}}) = \frac{V_{SO}^n(\varepsilon_{\text{lab}}) + V_{SO}^p(\varepsilon_{\text{lab}})}{2A} \quad (\text{C22})$$

W_{SO} likewise

In the expressions above, the superscript n (p) denotes the value of the corresponding quantity for an individual neutron (proton), e.g., $V_{SO}^n(\varepsilon_{\text{lab}})$ is the spin-orbit well depth for a neutron projectile.

-
- [1] K. Hirata, T. Kajita, M. Koshiba, M. Nakahata, Y. Oyama, N. Sato, A. Suzuki, M. Takita, Y. Totsuka, *et al.*, “Observation of a neutrino burst from the supernova SN1987A,” *Phys. Rev. Lett.* **58**, 1490–1493 (1987).
 - [2] E. N. Alekseev, L. N. Alekseeva, V. I. Volchenko, and I. V. Krivosheina, “Possible Detection of a Neutrino Signal on 23 February 1987 at the Baksan Underground Scintillation Telescope of the Institute of Nuclear Research,” *JETP Lett.* **45**, 589–592 (1987).
 - [3] R. M. Bionta, G. Blewitt, C. B. Bratton, D. Casper, A. Ciocio, R. Claus, B. Cortez, M. Crouch, S. T. Dye, S. Errede, *et al.*, “Observation of a neutrino burst in coincidence with supernova 1987A in the Large Magellanic Cloud,” *Phys. Rev. Lett.* **58**, 1494–1496 (1987).
 - [4] G. G. Raffelt, “What have we learned from SN 1987A?” *Mod. Phys. Lett. A* **05**, 2581–2592 (1990), <https://inspirehep.net/literature/295317>.
 - [5] R. Schaeffer, “SN 1987A. A Review,” *Acta Phys. Pol.* **21**, 357–376 (1990).
 - [6] B. Jegerlehner, F. Neubig, and G. Raffelt, “Neutrino oscillations and the supernova 1987A signal,” *Phys. Rev. D* **54**, 1194–1203 (1996), [arXiv:astro-ph/9601111](https://arxiv.org/abs/hep-ph/9601111).
 - [7] F. Vissani, “Comparative analysis of SN1987A antineutrino fluence,” *J. Phys. G* **42**, 013001 (2014), [arXiv:1409.4710](https://arxiv.org/abs/1409.4710).
 - [8] A. Mirizzi, I. Tamborra, H. Janka, N. Saviano, K. Scholberg, R. Bollig, L. Hudepohl, and S. Chakraborty, “Supernova neutrinos: production, oscillations and detection,” *Riv. Nuovo Cimento* **39**, 1–112 (2016), [arXiv:1508.00785](https://arxiv.org/abs/1508.00785).
 - [9] D. Branch and J. C. Wheeler, “Supernova 1987A,” in *Supernova Explosions* (Springer Berlin Heidelberg, Berlin, Heidelberg, 2017) Chap. 11, pp. 219–243.
 - [10] K. Scholberg, “Supernova neutrino detection,” *Annu. Rev. Nucl. Part. Sci.* **62**, 81–103 (2012), [arXiv:1205.6003](https://arxiv.org/abs/1205.6003).
 - [11] K. Rozwadowska, F. Vissani, and E. Cappellaro, “On the rate of core collapse supernovae in the milky way,” *New Astron.* **83**, 101498 (2021), [arXiv:2009.03438](https://arxiv.org/abs/2009.03438).
 - [12] B. Müller, “Neutrino emission as diagnostics of core-collapse supernovae,” *Annu. Rev. Nucl. Part. Sci.* **69**, 253–278 (2019), [arXiv:1904.11067](https://arxiv.org/abs/1904.11067).
 - [13] S. Horiuchi and J. P. Kneller, “What can be learned from a future supernova neutrino detection?” *J. Phys. G* **45**, 043002 (2018), [arXiv:1709.01515](https://arxiv.org/abs/1709.01515).
 - [14] G. G. Raffelt, “Supernova neutrino observations: What can we learn?” *Nucl. Phys. B, Proc. Suppl.* **221**, 218–229 (2011), [arXiv:astro-ph/0701677](https://arxiv.org/abs/astro-ph/0701677).
 - [15] B. Abi, R. Acciarri, M. A. Acero, G. Adamov, D. Adams, M. Adinolfi, Z. Ahmad, J. Ahmed, T. Alion, S. A. Monsalve, *et al.* (DUNE Collaboration), “Supernova neutrino burst detection with the Deep Underground Neutrino Experiment,” (2020), [arXiv:2008.06647](https://arxiv.org/abs/2008.06647).
 - [16] A. Ankowski, J. Beacom, O. Benhar, S. Chen, J. Cherry, Y. Cui, A. Friedland, I. Gil-Botella, A. Haghighat, S. Horiuchi, *et al.*, “Supernova physics at DUNE,” (2016), [arXiv:1608.07853](https://arxiv.org/abs/1608.07853).
 - [17] B. Abi, R. Acciarri, M. A. Acero, G. Adamov, D. Adams, M. Adinolfi, Z. Ahmad, J. Ahmed, T. Alion, S. A. Monsalve, *et al.* (DUNE Collaboration), “Volume I. Introduction to DUNE,” *J. Instrum.* **15**, T08008–T08008 (2020), [arXiv:2002.02967](https://arxiv.org/abs/2002.02967).
 - [18] S. W. Li, L. F. Roberts, and J. F. Beacom, “Exciting prospects for detecting late-time neutrinos from core-collapse supernovae,” *Phys. Rev. D* **103**, 023016 (2021), [arXiv:2008.04340](https://arxiv.org/abs/2008.04340).
 - [19] F. Capozzi, S. W. Li, G. Zhu, and J. F. Beacom, “DUNE as the next-generation solar neutrino experiment,” *Phys. Rev. Lett.* **123**, 131803 (2019), [arXiv:1808.08232](https://arxiv.org/abs/1808.08232).
 - [20] S. Tufanli (SBND Collaboration), “The SBND experiment,” *Proc. Sci. HQL* **2016**, 070 (2017).
 - [21] D. Brailsford (SBND Collaboration), “Physics program of the Short-Baseline Near Detector,” *J. Phys. Conf. Ser.* **888**, 012186 (2017).
 - [22] R. Acciarri, C. Adams, R. An, A. Aparicio, S. Aponte, J. Asaadi, M. Auger, N. Ayoub, L. Bagby, B. Baller, *et al.* (MicroBooNE Collaboration), “Design and construction of the MicroBooNE detector,” *J. Instrum.* **12**, P02017–P02017 (2017), [arXiv:1612.05824](https://arxiv.org/abs/1612.05824).
 - [23] S. Amerio, S. Amoroso, M. Antonello, P. Aprili, M. Armenante, F. Arneodo, A. Badertscher, B. Baiboussinov, M. Baldo Ceolin, G. Battistoni, *et al.*, “Design, construction and tests of the ICARUS T600 detector,” *Nucl. Instrum. Methods Phys. Res. A* **527**, 329–410 (2004).
 - [24] P. A. N. Machado, O. Palamara, and D. W. Schmitz, “The Short-Baseline Neutrino Program at Fermilab,” *Annu. Rev. Nucl. Part. Sci.* **69**, 363–387 (2019), [arXiv:1903.04608](https://arxiv.org/abs/1903.04608).
 - [25] R. Acciarri, C. Adams, R. An, C. Andreopoulos, A. M. Ankowski, M. Antonello, J. Asaadi, W. Badgett, L. Bagby, B. Baiboussinov, *et al.*, “A proposal for a three detector short-baseline neutrino oscillation program in the Fermilab Booster Neutrino Beam,” (2015), [arXiv:1503.01520](https://arxiv.org/abs/1503.01520).

- [26] P. Abratenko, M. Alrashed, R. An, J. Anthony, J. Asaadi, A. Ashkenazi, S. Balasubramanian, B. Baller, C. Barnes, G. Barr, *et al.* (MicroBooNE Collaboration), “The continuous readout stream of the MicroBooNE liquid argon time projection chamber for detection of supernova burst neutrinos,” *J. Instrum.* **16**, P02008 (2021), [arXiv:2008.13761](#).
- [27] C. Anderson, M. Antonello, B. Baller, T. Bolton, C. Bromberg, F. Cavanna, E. Church, D. Edmunds, A. Ereditato, S. Farooq, *et al.* (ArgoNeuT Collaboration), “The ArgoNeuT detector in the NuMI low-energy beam line at Fermilab,” *J. Instrum.* **7**, P10019–P10019 (2012), [arXiv:1205.6747](#).
- [28] R. Acciarri, C. Adams, J. Asaadi, B. Baller, T. Bolton, C. Bromberg, F. Cavanna, E. Church, D. Edmunds, A. Ereditato, S. Farooq, *et al.* (ArgoNeuT Collaboration), “Demonstration of MeV-scale physics in liquid argon time projection chambers using ArgoNeuT,” *Phys. Rev. D* **99**, 012002 (2019), [arXiv:1810.06502](#).
- [29] MicroBooNE Collaboration, “MeV Scale Physics in MicroBooNE,” MICROBOONE-NOTE-1076-PUB.
- [30] A. Friedland and S. W. Li, “Understanding the energy resolution of liquid argon neutrino detectors,” *Phys. Rev. D* **99**, 036009 (2019), [arXiv:1811.06159](#).
- [31] W. Castiglioni, W. Foreman, B. R. Littlejohn, M. Malaker, I. Lepetic, and A. Mastbaum, “Benefits of MeV-scale reconstruction capabilities in large liquid argon time projection chambers,” *Phys. Rev. D* **102**, 092010 (2020), [arXiv:2006.14675](#).
- [32] D. Akimov, J. B. Albert, P. An, C. Awe, P. S. Barbeau, B. Becker, V. Belov, I. Bernardi, M. A. Blackston, L. Blokland, *et al.* (COHERENT Collaboration), “First measurement of coherent elastic neutrino-nucleus scattering on argon,” *Phys. Rev. Lett.* **126**, 012002 (2021), [arXiv:2003.10630](#).
- [33] S. Ajimura, M. K. Cheoun, J. H. Choi, H. Furuta, M. Harada, S. Hasegawa, Y. Hino, T. Hiraiwa, E. Iwai, S. Iwata, *et al.*, “Technical Design Report (TDR): Searching for a Sterile Neutrino at J-PARC MLF (E56, JSNS²),” (2017), [arXiv:1705.08629](#).
- [34] S. Gardiner, *Nuclear Effects in Neutrino Detection*, Ph.D. thesis, University of California, Davis (2018).
- [35] N. Van Dessel, N. Jachowicz, and A. Nikolakopoulos, “Forbidden transitions in neutral- and charged-current interactions between low-energy neutrinos and argon,” *Phys. Rev. C* **100**, 055503 (2019), [arXiv:1903.07726](#).
- [36] N. Van Dessel, A. Nikolakopoulos, and N. Jachowicz, “Lepton kinematics in low-energy neutrino-argon interactions,” *Phys. Rev. C* **101**, 045502 (2020), [arXiv:1912.10714](#).
- [37] E. Kolbe, K. Langanke, S. Krewald, and F.-K. Thielemann, “Inelastic neutrino scattering on ¹²C and ¹⁶O above the particle emission threshold,” *Nucl. Phys. A* **540**, 599–620 (1992).
- [38] K. Langanke, P. Vogel, and E. Kolbe, “Signal for supernova ν_μ and ν_τ neutrinos in water Čerenkov detectors,” *Phys. Rev. Lett.* **76**, 2629 (1996), [arXiv:nucl-th/9511032v1](#).
- [39] E. Kolbe and K. Langanke, “Role of ν -induced reactions on lead and iron in neutrino detectors,” *Phys. Rev. C* **63**, 025802 (2001), [arXiv:nucl-th/0003060](#).
- [40] M.-K. Cheoun, E. Ha, T. Hayakawa, S. Chiba, K. Nakamura, T. Kajino, and G. J. Mathews, “Neutrino induced reactions for ν -process nucleosynthesis of ⁹²Nb and ⁹⁸Tc,” *Phys. Rev. C* **85**, 065807 (2012), [arXiv:1108.4229](#).
- [41] A. Bandyopadhyay, P. Bhattacharjee, S. Chakraborty, K. Kar, and S. Saha, “Detecting supernova neutrinos with iron and lead detectors,” *Phys. Rev. D* **95**, 065022 (2017), [arXiv:1607.05591](#).
- [42] D. Vale, T. Rauscher, and N. Paar, “Hybrid method to resolve the neutrino mass hierarchy by supernova (anti)neutrino induced reactions,” *J. Cosmol. Astropart. Phys.* **2016**, 007 (2016), [arXiv:1509.07342](#).
- [43] K. S. Kim and M.-K. Cheoun, “Roles of one-step process on neutrino scattering off ¹²C,” *Phys. Lett. B* **679**, 330–333 (2009).
- [44] M.-K. Cheoun and K. S. Kim, “One and two-step processes on the neutrino-nucleus scattering near nucleon threshold region,” *Int. J. Mod. Phys. Conf. Ser.* **01**, 171–176 (2011).
- [45] A. G. Flowers, A. C. Shotter, D. Branford, J. C. McGeorge, and R. O. Owens, “New evidence for a direct process in the (e, α) reaction,” *Phys. Rev. Lett.* **40**, 709–712 (1978).
- [46] S. Gardiner, “MARLEY (Model of Argon Reaction Low Energy Yields),” (2021), version 1.2.0.
- [47] S. Gardiner, “MARLEY User Guide,” <https://marleygen.org> (2021).
- [48] S. Gardiner, “Simulating low-energy neutrino interactions with MARLEY,” (2021), [arXiv:2101.11867](#).
- [49] J. Engel, “Approximate treatment of lepton distortion in charged-current neutrino scattering from nuclei,” *Phys. Rev. C* **57**, 2004–2009 (1998), [arXiv:nucl-th/9711045](#).
- [50] C. Volpe, N. Auerbach, G. Colò, and N. Van Giai, “Charged-current neutrino-²⁰⁸Pb reactions,” *Phys. Rev. C* **65**, 044603 (2002), [arXiv:nucl-th/0103039](#).
- [51] E. Ydrefors and J. Suhonen, “Charged-current neutrino-nucleus scattering off the even molybdenum isotopes,” *Adv. High Energy Phys.* **2012**, 373946 (2012).
- [52] E. Fermi, “Versuch einer Theorie der β -Strahlen. I.” *Z. Phys.* **88**, 161–177 (1934), in German.
- [53] F. L. Wilson, “Fermi’s theory of beta decay,” *Am. J. Phys.* **36**, 1150 (1968), English translation of ref. [52].
- [54] M. Cannoni, “Lorentz invariant relative velocity and relativistic binary collisions,” *Int. J. Mod. Phys. A* **32**, 1730002 (2017), [arXiv:1605.00569](#).
- [55] H. Berns, H. Chen, D. Cline, J. Danielson, Z. Djurcic, S. Elliott, G. Garvey, V. Gehman, C. Grant, E. Guardincerri, *et al.* (CAPTAIN Collaboration), “The CAPTAIN detector and physics program,” (2013), [arXiv:1309.1740](#).
- [56] W. Liu, M. Hellström, R. Collatz, J. Benlliure, L. Chulkov, D. C. Gil, F. Farget, H. Grawe, Z. Hu, N. Iwasa, M. Pfützner, A. Piechaczek, R. Raabe, I. Reusen, E. Roeckl, G. Vancraeynest, and A. Wöhr, “ β decay of ⁴⁰Ti and ⁴¹Ti and implication for solar-neutrino detection,” *Phys. Rev. C* **58**, 2677–2688 (1998).
- [57] M. Bhattacharya, A. García, N. I. Kaloskakis, E. G. Adelberger, H. E. Swanson, R. Anne, M. Lewitowicz, M. G. Saint-Laurent, W. Trinder, C. Donzaud, *et al.*, “Neutrino absorption efficiency of an ⁴⁰Ar detector from the β decay of ⁴⁰Ti,” *Phys. Rev. C* **58**, 3677–3687 (1998).
- [58] M. Bhattacharya, C. D. Goodman, and A. García, “Weak-interaction strength from charge-exchange reactions versus β decay in the $A = 40$ isoquintet,” *Phys.*

- Rev. C **80**, 055501 (2009).
- [59] C. D. Goodman, C. A. Goulding, M. B. Greenfield, J. Rapaport, D. E. Bainum, C. C. Foster, W. G. Love, and F. Petrovich, “Gamow-Teller matrix elements from $0^\circ(p, n)$ cross sections,” *Phys. Rev. Lett.* **44**, 1755–1759 (1980).
- [60] T. N. Taddeucci, J. Rapaport, D. E. Bainum, C. D. Goodman, C. C. Foster, C. Gaarde, J. Larsen, C. A. Goulding, D. J. Horen, T. Masterson, and E. Sugarbaker, “Energy dependence of the ratio of isovector effective interaction strengths $\left|\frac{J_{\sigma\pi}}{J_\pi}\right|$ from $0^\circ(p, n)$ cross sections,” *Phys. Rev. C* **25**, 1094–1097 (1982).
- [61] T. N. Taddeucci, C. A. Goulding, T. A. Carey, R. C. Byrd, C. D. Goodman, C. Gaarde, J. Larsen, D. Horen, J. Rapaport, and E. Sugarbaker, “The (p, n) reaction as a probe of beta decay strength,” *Nucl. Phys. A* **469**, 125–172 (1987).
- [62] C. D. Goodman, M. Bhattacharya, M. B. Aufderheide, S. D. Bloom, and P. Zupranski, “Data analysis techniques for extracting Gamow-Teller strengths from $0^\circ(p, n)$ data,” *Nucl. Instrum. Methods Phys. Res. A* **462**, 545–554 (2001).
- [63] D. Frekers, P. Puppe, J. H. Thies, and H. Ejiri, “Gamow-Teller strength extraction from $(^3\text{He}, t)$ reactions,” *Nucl. Phys. A* **916**, 219–240 (2013).
- [64] J. Chen, “Nuclear data sheets for $A = 40$,” *Nucl. Data Sheets* **140**, 1–376 (2017).
- [65] “ENSDF: Evaluated Nuclear Structure Data File,” <https://www.nndc.bnl.gov/ensdf/> (2021).
- [66] J. K. Tuli, *Evaluated Nuclear Structure Data File: A Manual for Preparation of Data Sets*, Tech. Rep. BNL-NCS-51655-01/02-Rev (National Nuclear Data Center, Brookhaven National Laboratory).
- [67] M. Karakoç, R. G. T. Zegers, B. A. Brown, Y. Fujita, T. Adachi, I. Boztosun, H. Fujita, M. Csatlós, J. M. Deaven, C. J. Guess, *et al.*, “Gamow-Teller transitions in the $A = 40$ isoquintet of relevance for neutrino captures in ^{40}Ar ,” *Phys. Rev. C* **89**, 064313 (2014).
- [68] K. Ikeda, S. Fujii, and J. I. Fujita, “The (p, n) reactions and beta decays,” *Phys. Lett.* **3**, 271–272 (1963).
- [69] M.-K. Cheoun, E. Ha, and T. Kajino, “High-lying excited states in Gamow Teller strength and their roles in neutrino reactions,” *Eur. Phys. J. A* **48**, 137 (2012).
- [70] P. J. Mohr, B. N. Taylor, and D. B. Newell, “CODATA recommended values of the fundamental physical constants: 2010,” *Rev. Mod. Phys.* **84**, 1527–1605 (2012).
- [71] G. Audi, M. Wang, A. H. Wapstra, F. G. Kondev, M. MacCormick, X. Xu, and B. Pfeiffer, “The AME2012 atomic mass evaluation,” *Chin. Phys. C* **36**, 1287–1602 (2012).
- [72] W. D. Myers and W. J. Swiatecki, “Nuclear masses and deformations,” *Nucl. Phys.* **81**, 1–60 (1966).
- [73] A. J. Koning, S. Hilaire, and S. Goriely, “Global and local level density models,” *Nucl. Phys. A* **810**, 13–76 (2008).
- [74] A. J. Koning, S. Hilaire, and M. C. Duijvestijn, “TALYS-1.0,” in *Proceedings of the International Conference on Nuclear Data for Science and Technology 2007*, edited by O. Bersillon, F. Gunsing, E. Bauge, R. Jacqmin, and S. Leraf (EDP Sciences, Les Ulis, France, 2008) pp. 211–214.
- [75] A. J. Koning and D. Rochman, “Modern nuclear data evaluation with the TALYS code system,” *Nucl. Data Sheets* **113**, 2841–2934 (2012).
- [76] A. Koning, S. Hilaire, and S. Goriely, *TALYS-1.6: A nuclear reaction program*, Nuclear Research and Consultancy Group (NRG) ().
- [77] A. Koning, S. Hilaire, and S. Goriely, *TALYS-1.95: A nuclear reaction program* ().
- [78] R. Capote, M. Herman, P. Obložinský, P. G. Young, S. Goriely, T. Belgia, A. V. Ignatyuk, A. J. Koning, S. Hilaire, V. A. Plujko, *et al.*, “RIPL – Reference Input Parameter Library for calculation of nuclear reactions and nuclear data evaluations,” *Nucl. Data Sheets* **110**, 3107–3214 (2009).
- [79] V. Weisskopf, “Statistics and nuclear reactions,” *Phys. Rev.* **52**, 295 (1937).
- [80] M. Herman, R. Capote, B. V. Carlson, P. Obložinský, M. Sin, A. Trkov, H. Wienke, and V. Zerkin, “EMPIRE: nuclear reaction model code system for data evaluation,” *Nucl. Data Sheets* **108**, 2655–2715 (2007).
- [81] O. Iwamoto, N. Iwamoto, S. Kunieda, F. Minato, and K. Shibata, “The CCONE code system and its application to nuclear data evaluation for fission and other reactions,” *Nucl. Data Sheets* **131**, 259 – 288 (2016), Special Issue on Nuclear Reaction Data.
- [82] T. Kawano, P. Talou, M. B. Chadwick, and T. Watanabe, “Monte Carlo simulation for particle and γ -ray emissions in statistical Hauser-Feshbach model,” *J. Nucl. Sci. Technol.* **47**, 462–469 (2010).
- [83] W. Hauser and H. Feshbach, “The inelastic scattering of neutrons,” *Phys. Rev.* **87**, 366 (1952).
- [84] A. J. Cole, *Statistical Models for Nuclear Decay: From Evaporation to Vaporization*, Series in Fundamental and Applied Nuclear Physics (CRC Press, 2000).
- [85] I. J. Thompson and F. M. Nunes, *Nuclear Reactions for Astrophysics: Principles, Calculation and Applications of Low-Energy Reactions* (Cambridge University Press, 2009).
- [86] A. J. Koning and J. P. Delaroche, “Local and global nucleon optical models from 1 keV to 200 MeV,” *Nucl. Phys. A* **713**, 231–310 (2003).
- [87] F. W. J. Olver, A. B. Olde Daalhuis, D. W. Lozier, B. I. Schneider, R. F. Boisvert, C. W. Clark, B. R. Miller, B. V. Saunders, H. S. Cohl, and M. A. McClain, eds., “*NIST Digital Library of Mathematical Functions*,” Release 1.1.1 of 2021-03-15 (2021).
- [88] D. M. Brink, *Some aspects of the interaction of light with matter*, Ph.D. thesis, Oxford University (1955).
- [89] P. Axel, “Electric dipole ground-state transition width strength function and 7-MeV photon interactions,” *Phys. Rev.* **126**, 671 (1962).
- [90] T. Belgia, O. Bersillon, R. Capote Noy, T. Fukahori, G. Zhigang, S. Goriely, M. Herman, A. V. Ignatyuk, S. Kailas, A. Koning, *et al.*, *Handbook for calculations of nuclear reaction data, RIPL-2*, Tech. Rep. IAEA-TECDOC-1506 (International Atomic Energy Agency, 2006).
- [91] International Atomic Energy Agency, *Reference Input Parameter Library: Handbook for calculations of nuclear reaction data*, Tech. Rep. IAEA-TECDOC-1034.
- [92] A. Nikrant, R. Laha, and S. Horiuchi, “Robust measurement of supernova ν_e spectra with future neutrino detectors,” *Phys. Rev. D* **97**, 023019 (2018), arXiv:1711.00008.
- [93] T. S. Kosmas, D. K. Papoulias, M. Tórtola, and J. W. F. Valle, “Probing light sterile neutrino signa-

- tures at reactor and Spallation Neutron Source neutrino experiments,” *Phys. Rev. D* **96**, 063013 (2017), [arXiv:1703.00054](#).
- [94] A. Bolozdynya, F. Cavanna, Y. Efremenko, G. T. Garvey, V. Gudkov, A. Hatzikoutelis, W. R. Hix, W. C. Louis, J. M. Link, D. M. Markoff, *et al.*, “Opportunities for neutrino physics at the Spallation Neutron Source: a white paper,” (2012), [arXiv:1211.5199](#).
- [95] J. D. Walecka, “Semileptonic weak interactions in nuclei,” in *Muon Physics, Volume II: Weak Interactions*, edited by V. W. Hughes and C. S. Wu (Academic Press, 1975) pp. 113–218.
- [96] E. Kolbe, K. Langanke, G. Martínez-Pinedo, and P. Vogel, “Neutrino-nucleus reactions and nuclear structure,” *J. Phys. G* **29**, 2569–2596 (2003), [arXiv:nucl-th/0311022v1](#).
- [97] D. Akimov, J. B. Albert, *et al.* (COHERENT Collaboration), “COHERENT 2018 at the Spallation Neutron Source,” (2018), [arXiv:1803.09183](#).
- [98] A. Klinskih, V. Egorov, M. Shirchenko, D. Zinatulina, O. Civitarese, I. Stekl, and J. Suhonen, “Muon capture in ^{40}Ar . Muon life-time and isotope yields.” *AIP Conf. Proc.* **942**, 49–51 (2007).
- [99] M. Pârvu, A. Chiriacescu, and I. Lazanu, “Short analysis of cosmogenic production of radioactive isotopes in argon as target for the next neutrino experiments,” *Radiat. Phys. Chem.* **152**, 129–136 (2018), [arXiv:1712.04399](#).
- [100] J. Heeck and V. Takhistov, “Inclusive nucleon decay searches as a frontier of baryon number violation,” *Phys. Rev. D* **101**, 015005 (2020), [arXiv:1910.07647](#).
- [101] Z. Djurcic, A. Fiorentini, M. Goodman, D. M. Caicedo, A. Rafique, J. R. Rondon, and S. Yu, “Searches for proton-decay with additional signatures from nuclear deexcitations and with precise timing from photon-detectors in large LArTPCs,” *Snowmass 2021 letter of interest*.
- [102] J. A. Dror, G. Elor, and R. McGehee, “Directly detecting signals from absorption of fermionic dark matter,” *Phys. Rev. Lett.* **124**, 181301 (2020), [arXiv:1905.12635](#).
- [103] J. A. Dror, G. Elor, and R. McGehee, “Absorption of fermionic dark matter by nuclear targets,” *J. High Energy Phys.* **2020**, 1–38 (2020), [arXiv:1908.10861](#).
- [104] A. V. Ignatyuk, G. N. Smirenkin, and A. S. Tishin, “Phenomenological description of energy dependence of the level density parameter,” *Yad. Fiz.* **21**, 485–490 (1975), in Russian.
- [105] M. Wang, G. Audi, A. H. Wapstra, F. G. Kondev, M. MacCormick, X. Xu, and B. Pfeiffer, “The AME2012 atomic mass evaluation: (II). Tables, graphs and references,” *Chin. Phys. C* **36**, 1603 (2012).
- [106] A. Mengoni and Y. Nakajima, “Fermi-gas model parametrization of nuclear level density,” *J. Nucl. Sci. Technol.* **31**, 151–162 (1994).
- [107] H. A. Bethe, “Nuclear physics B. nuclear dynamics, theoretical,” *Rev. Mod. Phys.* **9**, 69 (1937).
- [108] S. I. Al-Quraishi, S. M. Grimes, T. N. Massey, and D. A. Resler, “Level densities for $20 \leq A \leq 110$,” *Phys. Rev. C* **67**, 015803 (2003).
- [109] R. D. Woods and D. S. Saxon, “Diffuse surface optical model for nucleon-nuclei scattering,” *Phys. Rev.* **95**, 577 (1954).
- [110] D. G. Madland, “Recent results in the development of a global medium-energy nucleon-nucleus optical-model potential,” in *Proceedings of a Specialists’ Meeting on Preequilibrium Nuclear Reactions*, NEA/NEANDC(1988)245/U, pp. 103–110.